Multi-Detector CT Imaging Handbook

Multi-Detector CT Imaging

Principles, Head, Neck, and Vascular Systems

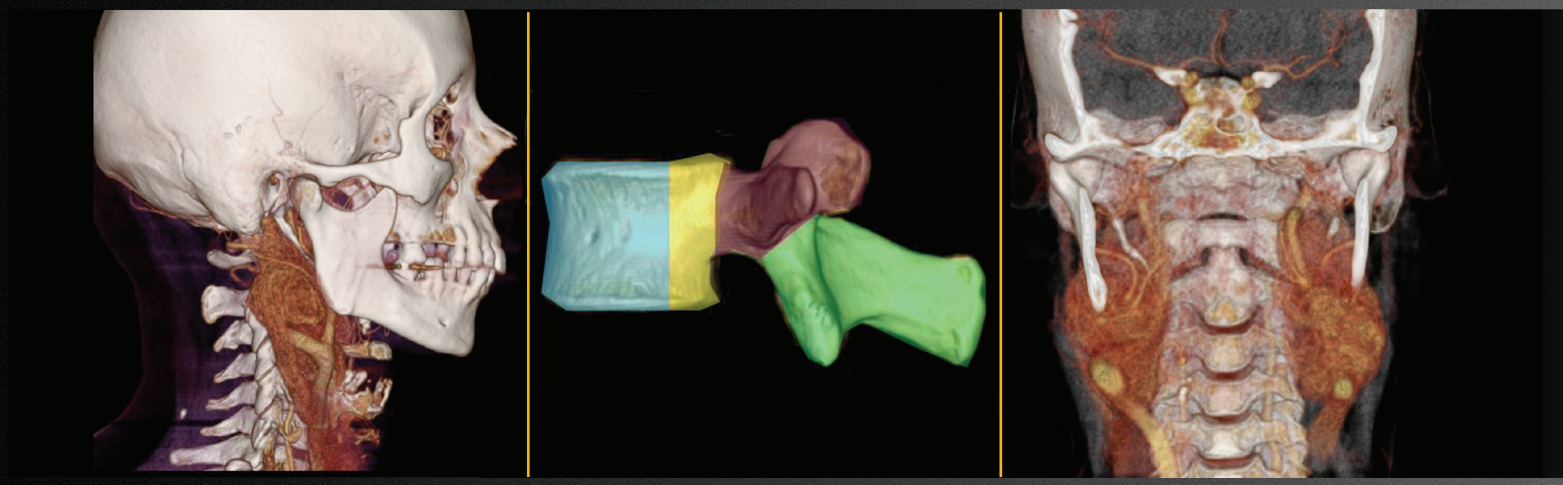

edited by
Luca Saba • Jasjit S. Suri

CRC Press
Taylor & Francis Group

Multi-Detector CT Imaging Handbook

Multi-Detector CT Imaging

Principles, Head, Neck, and Vascular Systems

Multi-Detector CT Imaging Handbook

Multi-Detector CT Imaging: Principles, Head, Neck, and Vascular Systems

Multi-Detector CT Imaging: Abdomen, Pelvis, and CAD Applications

Multi-Detector CT Imaging

Principles, Head, Neck, and Vascular Systems

edited by
Luca Saba • Jasjit S. Suri

CRC Press
Taylor & Francis Group
Boca Raton London New York

CRC Press is an imprint of the
Taylor & Francis Group, an **informa** business

CRC Press
Taylor & Francis Group
6000 Broken Sound Parkway NW, Suite 300
Boca Raton, FL 33487-2742

Version Date: 20121214

International Standard Book Number-13: 978-1-4398-9384-5 (eBook - PDF)

Luca Saba dedicates this book to his parents

Giovanni Saba and Raffaela Polla for their love.

Jasjit S. Suri dedicates this book to his children

Harman Suri and Neha Suri for their love.

Contents

Section III Cardiovascular System

Section IV Thorax and Mediastinum

Foreword

Medical imaging, and computed tomography (CT) in particular, have revolutionized medical care over the past four decades in ways unimaginable prior to the introduction of CT. The impact of CT extends over virtually every clinical field and region of the body, and through all aspects of care including screening, diagnosis and problem solving, monitoring disease progression and treatment responses, and directing minimally invasive procedural interventions. It is no wonder then, with the critical role CT plays, and with the rapid innovations in computer technology, that advances in the capabilities and complexity of CT imaging continue to evolve. An up-to-date complete and authoritative educational and reference volume covering the entire spectrum of CT is a difficult task to accomplish and lacking in the radiology literature. *Multi-Detector CT Imaging*, edited by Dr. Luca Saba and Dr. Jasjit Suri, excels in meeting this need.

Drs. Saba and Suri have brought together an outstanding collection of international authors recognized worldwide as leaders in their fields. Their extensive clinical experience and practical knowledge are logically presented, well organized, and brilliantly visualized. The two books in this set are amazingly complete in content, depth, and quality, yet read easily as an educational introduction or as a reference source.

The value of these books will be appreciated by readers in many ways. They cover all aspects of CT imaging, with technical principles and postprocessing methodologies comprehensibly presented, and extensive clinical specialty chapters easily searchable for specific information without need of an index. The value goes far beyond just a "how-to" or an encyclopedia of findings, however. The authors have uniformly put techniques, clinical findings, pathologic disease presentations, and clinical implications of imaging findings in practical perspective. The organization of the chapters is a wonderful progression that actually follows how the radiologist approaches unknown cases. Most chapters start with a review of imaging techniques for the organ or disease process. This is often followed with a practical discussion reviewing the spectrum of abnormal CT findings and their significance and differential diagnosis, followed subsequently by thorough material organized around understanding disease processes. Helpful correlative material with MRI and PET imaging is frequently presented to illustrate how these modalities complement each other.

This resource is a remarkable tool that will be of value to imaging professionals from every clinical vantage point and will serve well those experienced with CT or those using it to first learn about CT. I personally look forward to using this resource and having it available for our trainees, not only as an essential educational tool, but knowing that it will stimulate our community to further push the frontiers of CT imaging.

Richard L. Baron, MD
Dean for Clinical Practice
Professor of Radiology
University of Chicago Pritzker School of Medicine

Preface

The introduction of multi-detector row computed tomography (CT) in the early 1990s resulted in a fundamental and far-reaching improvement of CT imaging. For the first time, volumes of data could be acquired without misregistration of anatomical details, which indicated the development of 3D image processing techniques. In the last 20 years, CT technology has further improved with the introduction of systems up to 320-detector rows and with the development of dual-source and multispectral technology.

From these developments, the diagnostic potential of CT has impressively improved with an exceptional spatial resolution and the possibility to analyze with an exquisite level of detail several kinds of pathology. Thanks to the development of CT perfusion technique, functional brain imaging as well as liver imaging is now possible.

The purpose of this book is to cover clinical and engineering benefits in the diagnosis of human pathologies. It discusses the protocols and potential of advanced computed tomography scanners, explaining easily, but with an adequate level of detail, the role and potential of CT.

Acknowledgments

It is not possible to overstate our gratitude to the many individuals who helped to produce this book. In particular, Luca Saba would like to thank Professors Giorgio Mallarini and Giancarlo Caddeo, who first taught him the principles of computed tomography. Dr. Saba also thanks Stefano Marcia, Paolo Siotto, and Giovanni Argiolas and his many colleagues, residents, students, and friends for their continuous exchanges during these years. A special thanks also to Carlo Nicola de Cecco for his help. Finally, Dr. Saba would like to acknowledge the patience and understanding displayed by Tiziana throughout his work. Without her continuous encouragement, this book would not have been completed.

Jasjit S. Suri acknowledges Dr. Luca Saba for his continuous dedication in the field of computer tomography imaging and his willingness to participate in successfully launching this project. Dr. Suri also thanks his family, Malvika, Harman, and Neha, who are always a source of shine and laughter. Special thanks to all his friends and collaborators around the world who helped commercialize medical devices and healthcare imaging products over the course of years.

Both editors have received considerable support and cooperation from individuals at CRC/Taylor & Francis, particularly Michael Slaughter, Jessica Vakili, Joette Lynch, Michele Smith and from Dennis Troutman at diacriTech, each of whom helped to minimize the obstacles that the editors encountered.

Editors

Luca Saba earned his MD from the University of Cagliari, Italy, in 2002. Today, he works in the University of Cagliari School of Medicine. His research fields are focused on multi-detector row computed tomography, magnetic resonance, ultrasound, neuroradiology, and diagnostics in vascular sciences.

His works, as lead author, have appeared in more than 100 high impact factor, peer-reviewed journals such as the*American Journal of Neuroradiology*, *European Radiology*, *European Journal of Radiology*, *Acta Radiologica*, *Cardiovascular and Interventional Radiology*, *Journal of Computer Assisted Tomography*, *American Journal of Roentgenology*, *Neuroradiology*, *Clinical Radiology*, *Journal of Cardiovascular Surgery*, and *Cerebrovascular Diseases*. He is a well-known speaker and has spoken over 45 times at national and international levels.

Dr. Saba has won 12 scientific and extracurricular awards during his career. He has presented more than 430 papers and posters at national and international congresses (RSNA, ESGAR, ECR, ISR, AOCR, AINR, JRS, SIRM, AINR). He has written eight book chapters, and he is currently serving as an editor of four books in the field of cardiovascular and neurodegenerative imaging.

He is a member of the Italian Society of Radiology, European Society of Radiology, Radiological Society of North America, American Roentgen Ray Society, and European Society of Neuroradiology.

Jasjit S. Suri earned his MS in neurological MRI from the University of Illinois, a PhD in cardiac imaging from the University of Washington and an MBA from the Weatherhead School of Management, Case Western Reserve University. He has worked as scientist, manager, senior director, vice president, and chief technology officer at IBM, Siemens Medical, Philips Healthcare, Fisher, and Eigen Inc.

He has written over 400 publications, 60 patents, 4 FDA clearances, and more than 25 books in medical imaging and biotechnologies (diagnostic and therapeutic). Dr. Suri has had a leadership role in releasing products in the men's and women's market in the fields of cardiology, neurology, urology, vascular, ophthalmology, and breast cancer.

Dr. Suri has received the President's Gold Medal and Fellow of American Institute of Medical and Biological Engineering from the National Academy of Sciences. He has won over 50 awards during his career. Dr. Suri is also a strategic advisory board member for more than half a dozen industries and international journals focused on biomedical imaging and technologies.

Contributors

Michele Anzidei
Department of Radiological Sciences
Sapienza University of Rome
Rome, Italy

Philip A. Araoz
Mayo Clinic
Rochester, Minnesota

Irene Ariozzi
Department of Surgical Sciences
University of Parma University Hospital
Parma, Italy

Asim K. Bag
Department of Radiology
Neuroradiology Section
The University of Alabama at Birmingham
Birmingham, Alabama

Glenn Bauman
Schulich School of Medicine and Dentistry
Western University
and
London Regional Cancer Program
London Health Sciences Centre
London, Ontario, Canada

Luca Bertaccini
Department of Radiological Sciences
Sapienza University of Rome
Rome, Italy

Samuel Boynton
Department of Radiology
Mayo Clinic
Rochester, Minnesota

Carlo Catalano
Department of Radiological Sciences
Sapienza University of Rome
Rome, Italy

Irfan Celebi
Department of Radiology
Sisli Etfal Training and Research Hospital
Istanbul, Turkey

Philip R. Chapman
Neuroradiology Section
Department of Radiology
The University of Alabama at Birmingham
Birmingham, Alabama

Joel K. Curé
Neuroradiology Section
Department of Radiology
University of Alabama at Birmingham
Birmingham, Alabama

Christopher D. d'Esterre
Imaging Program
Lawson Health Research Institute
London, Ontario, Canada

Tobias De Zordo
Department of Radiology
Medical University Innsbruck
Innsbruck, Austria

Pier Luigi Di Paolo
Department of Neurology and Psychiatry
Sapienza University
Rome, Italy

Robert Donnino
Departments of Medicine and Radiology
NYU School of Medicine
and
Veterans Affairs New York Harbor Healthcare System
New York, New York

Shehanaz Ellika
Neuroradiology Section
Department of Radiology
Boston Children Hospital
Harvard Medical School
Boston, Massachusetts

Gudrun Feuchtner
Department of Radiology
Medical University Innsbruck
Innsbruck, Austria

Francesco Fraioli
Department of Radiological Sciences
Sapienza University of Rome
Rome, Italy

Jorge M. Fuentes-Orrego
Harvard Medical School
and
Division of Abdominal Imaging and Intervention
Radiology Department
Massachusetts General Hospital
Boston, Massachusetts

Jin Mo Goo
Department of Radiology
Seoul National University College of Medicine
Seoul, Korea

Kheng-Thye Ho
Mount Alvernia Hospital
Singapore

Angelika Hoffmann
Department of Radiology
University of Virginia
Charlottesville, Virginia

Werner Jaschke
Department of Radiology
Medical University Innsbruck
Innsbruck, Austria

Nikolaj K. G. Jensen
Western University
London, Ontario, Canada

Jeffrey P. Kanne
Section of Thoracic Imaging
University of Wisconsin School of Medicine and Public Health
Madison, Wisconsin

Ting-Yim Lee
Lawson Health Research Institute
and
Robarts Research Institute
and
Diagnostic Imaging
St. Joseph's Healthcare London
and
Medical Imaging
Schulich School of Medicine and Dentistry
Western University
London, Ontario, Canada

Christianne Leidecker
Siemens Healthcare
Malvern, Pennsylvania

Michael M. Lell
Department of Radiology
Erlangen University Hospital
University of Erlangen-Nuremberg
Erlangen, Germany

Carmelinda Manna
Department of Surgical Sciences
University of Parma University Hospital
Parma, Italy

Eugenio Marotta
Department of Radiological Sciences
Sapienza University of Rome
Rome, Italy

Kosuke Matsubara
Department of Quantum Medical Technology
Faculty of Health Sciences
Kanazawa University
Kanazawa, Japan

Alessandro Napoli
Department of Radiological Sciences
Sapienza University of Rome
Rome, Italy

Karoline Netzer
Department of Radiology
Medical University Innsbruck
Innsbruck, Austria

Yousef W. Nielsen
Department of Radiology
University Hospital at Herlev
Copenhagen, Denmark

Jonathan K. Park
David Geffen School of Medicine at UCLA
and
Ronald Reagan UCLA Medical Center
Los Angeles, California

Antonio Pavarani
Department of Surgical Sciences
University of Parma University Hospital
Parma, Italy

Rocío Pérez-Johnston
Harvard Medical School
and
Division of Abdominal Imaging and Intervention
Radiology Department
Massachusetts General Hospital
Boston, Massachusetts

Whitney Pope
David Geffen School of Medicine at UCLA
and
Ronald Reagan UCLA Medical Center
Los Angeles, California

Eytan Raz
Department of Radiology
New York University School of Medicine
New York, New York

and

Department of Neurology and Psychiatry
Sapienza University
Rome, Italy

Ahmed Abdel Khalek Abdel Razek
Department of Diagnostic Radiology
Mansoura Faculty of Medicine
Mansoura, Egypt

Luca Saba
Department of Radiology
University of Cagliari
School of Medicine
Cagliari, Italy

Dushyant V. Sahani
Harvard Medical School
and
Division of Abdominal Imaging and Intervention
Radiology Department
Massachusetts General Hospital
Boston, Massachusetts

Paul Schoenhagen
Cleveland Clinic Lerner College of Medicine
Case Western University
and
Imaging Institute and Heart & Vascular Institute
Cleveland Clinic
Cleveland, Ohio

Goffredo Serra
Department of Radiological Sciences
Sapienza University of Rome
Rome, Italy

Aaron So
Imaging Program
Lawson Health Research Institute
and
Diagnostic Imaging
St. Joseph's Healthcare London
London, Ontario, Canada

Monvadi B. Srichai
Medstar Georgetown University Hospital
and
Medstar Heart Institute
Washington, DC

Errol E. Stewart
Imaging Program
Lawson Health Research Institute
and
Diagnostic Imaging
St. Joseph's Healthcare London
London, Ontario, Canada

Zhonghua Sun
Department of Imaging and Applied Physics
Curtin University
Perth, Australia

Jasjit S. Suri
Division of Diagnosis and Monitoring
AtheroPoint™ LLC.
Roseville, California

and

Department of Biomedical Engineering
Idaho State University
Pocatello, Idaho

Nicola Sverzellati
Department of Surgical Sciences
University of Parma University Hospital
Parma, Italy

Ahmed M. Tawfik
Diagnostic and Interventional Radiology Department
Mansoura Faculty of Medicine
Mansoura, Egypt

and

Department of Diagnostic and Interventional Radiology
J. W. Goethe University Hospital
Frankfurt, Germany

Henrik S. Thomsen
Department of Radiology
University Hospital at Herlev
and
Department of Diagnostic Sciences, Faculty of Health Sciences
University of Copenhagen
Copenhagen, Denmark

Surjith Vattoth
Department of Radiology
Neuroradiology Section
University of Alabama at Birmingham
Birmingham, Alabama

Thomas J. Vogl
Department of Diagnostic and Interventional Radiology
J. W. Goethe University Hospital
Frankfurt, Germany

Max Wintermark
Department of Radiology
University of Virginia
Charlottesville, Virginia

Eugene Wong
Schulich School of Medicine and Dentistry
Western University
and
London Regional Cancer Program
London Health Sciences Centre
London, Ontario, Canada

Timothy Pok Chi Yeung
Schulich School of Medicine and Dentistry
Western University
and
London Regional Cancer Program
London Health Sciences Centre
London, Ontario, Canada

Eleonora Zambrini
Department of Surgical Sciences
University of Parma University Hospital
Parma, Italy

Section I

General Principles

1

Technical Principles of Computed Tomography

Michael M. Lell and Christianne Leidecker

CONTENTS

1.1 Introduction

Computed tomography (CT) was introduced in the early 1970s with the first commercial scanner available in 1972 from EMI Laboratories (Hayes, UK). Since then, it has revolutionized diagnostic imaging. CT combined a computer to a medical imaging device, heralding a new era of digital imaging, and was the first technology to acquire and display cross-sectional x-ray images.

The first CT scanner, developed by the English engineer G.N. Hounsfield, was introduced as a pure head scanner with a conventional x-ray tube and a dual-row detector system moving incrementally around the patient. It was able to acquire 12 slices, each 13 mm thick, and reconstruct the images with a matrix of 80 × 80 pixels in approximately 35 minutes. Today, the whole brain can be visualized with high quality from a 10-second scan.

Although the performance of CT scanners increased with the progress in engineering, it was the introduction of helical (or spiral) CT in the early 1990s [1,2] that constituted a fundamental evolutionary step in the development and ongoing refinement of CT imaging techniques. Theoretically proposed several years before [3,4], spiral CT requires the continuous rotation of the x-ray tube and the detector. This was enabled through the introduction of slip-ring technology, with continuous power transmission to and data extraction off the rotating gantry (Figure 1.1). Spiral CT enabled the acquisition of volume data, thus avoiding misregistration or double registration of anatomical details. Additionally, longitudinal resolution could be improved through overlapping image reconstruction, since images can be reconstructed at any position along the patient axis (longitudinal axis, *z*-axis).

The introduction of multislice CT in 1998 constituted a milestone with regard to increased scan speed, improved *z*-axis spatial resolution, and better use of the available x-ray power. With single-slice spiral CT, the main drawbacks are insufficient volume coverage within one breath-hold time and reduced longitudinal spatial resolution because of wide collimation. Isotropic resolution, that is, equal resolution in all three spatial directions, could be achieved for only very limited scan ranges in single-slice spiral CT [5]. Four-slice CT systems, made available by all major CT manufacturers in 1998 [6,7], allowed for increased volume coverage in shorter scan times and improved longitudinal resolution. Despite promising advances, clinical challenges and limitations remained for four-slice CT systems. True isotropic resolution for routine applications could not be achieved for many applications requiring extended scan ranges, since wider collimated slices (4 × 2.5 mm or 4 × 3.75 mm) had to be chosen to complete the scan within a reasonable time frame. Although four-slice CT systems with rotation times as short as 0.5 second enabled venturing into the realms of cardiac imaging [8,9], reliable imaging of patients with higher heart rates was not possible because of limited temporal resolution. In addition, insufficient longitudinal resolution and associated partial volume artifacts limited the imaging of stents or severely calcified arteries [10].

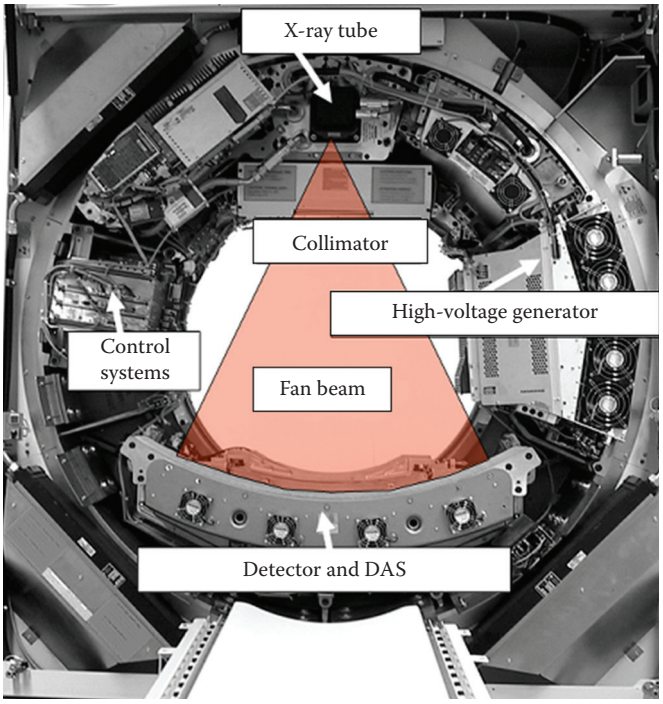

FIGURE 1.1
Basic components of a third-generation computed tomography system: unlike first-generation systems with a collimated pencil beam or second-generation systems with a small fan beam, the fan beam of a third-generation scanner covers the whole object and a pure rotational motion of the tube–detector unit can be performed instead of translation and rotation. DAS = data acquisition system.

As a next step, the introduction of 16-slice CT systems enabled routine acquisition of large anatomical volumes with isotropic submillimeter spatial resolution. With further reduced rotation times and larger volume coverage, examination times could be significantly reduced for standard protocols or, alternatively, scan ranges could be significantly extended.

The routine acquisition of volume data became the basis for advanced applications such as CT angiography (CTA), which allows noninvasive assessment of vascular disease. Volume data was the prerequisite for the development of three-dimensional (3D) image-processing techniques such as multiplanar reformats (MPRs), curved multiplanar reformats (CPRs), maximum intensity projections (MIPs), shaded surface displays (SSDs), volume rendering techniques (VRTs), and image registration techniques, which are an indispensable tool in image evaluation today [11].

In 2004, the first generation of 64-slice CT systems was introduced. Two different scanner concepts were proposed by different vendors. The first was the so-called "volume concept" that aimed at a further increase in volume coverage speed by using 64 detector rows instead of 16 without changing the physical parameters of the scanner compared to the respective 16-slice version. The second was the "resolution concept," which uses 32 physical detector rows in combination with a refined *z*-sampling technique. Double *z*-sampling is enabled by a periodic motion of the focal spot in the *z*-direction with the goal to simultaneously acquire 64 overlapping slices with pitch-independent increase of longitudinal resolution and reduction of spiral artifacts. Along with increased volume coverage, temporal resolution was improved with gantry rotation times of 0.33 second. For the first time, CT had the potential to robustly image the heart even at higher heart rates, thereby significantly reducing the number of patients with unevaluable coronary segments and facilitating the successful integration of coronary CTA into routine clinical algorithms.

The "slice war" continued and today's high-end single-source scanners can acquire up to 256 slices with an isotropic resolution down to 0.3 mm. Rotation times are as low as 0.27 second with a corresponding temporal resolution of 135 ms. The "volume CT" concept utilizes 320 detectors at 0.5 mm thickness and a coverage of 16 cm at isocenter.

Dual-source CT (DSCT) systems were introduced in 2005 [12]. As the name implies, the system uses two x-ray tubes and two corresponding detectors offset by 90° (Figure 1.2). With a DSCT system, temporal resolution equals a quarter of the gantry rotation time, independent of the patient's heart rate. Hence, one of the key benefits of DSCT scanners lies in cardiac imaging. Alternatively, the simultaneous operation of both tubes provides higher power reserves for fast imaging in obese patients, or the x-ray tubes can be operated at different tube voltages and/or different prefiltration, allowing dual energy acquisitions. Potential applications of dual-energy CT (DECT) include tissue characterization, calcium quantification, and quantification of the local blood volume in contrast-enhanced scans. In the meantime, second-generation DSCT scanners are available; wider detectors with 128 slices, further increased rotation speed, and new high-pitch scan modes enable further improvements in cardiac CT and DECT along with a significant dose reduction potential.

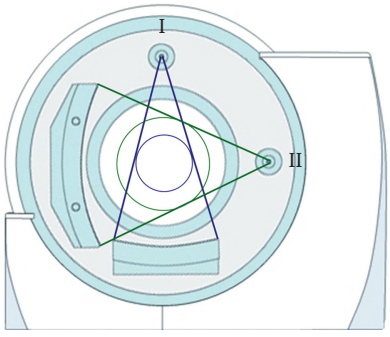

FIGURE 1.2
Schematic illustration of a dual-source CT (DSCT) system using two tubes and two corresponding detectors offset by 90° or 95°: the systems available commercially have one detector (I) that is restricted to a smaller, central field of view (26 or 33 cm, blue circle) and one detector (II) that covers the entire scan field of view (green circle).

1.2 Basic Physics and Image Reconstruction

The fundamental principle in CT imaging lies in measuring the two-dimensional (2D) distribution of x-ray attenuation coefficient μ. The linear attenuation coefficient μ is characteristic for the material and the energy of the photons. Assuming a primary x-ray photon intensity I_0, μ determines the measured photon intensity I behind an object of thickness d. For the simple case of monoenergetic photons and a homogeneous object, this is given by a simple exponential relationship:

$$I = I_0 e^{-\mu d} \tag{1.1}$$

With μ being characteristic of the attenuating material, it is therefore possible to distinguish materials with different attenuation coefficients. In CT, the goal is to obtain the distribution of attenuation coefficients for any given slice, $\mu(x, y)$. For an image with n^2 pixels and thus a 2D distribution of attenuation coefficients with n^2 values, one needs at least n^2 independently measured intensities I in Equation 1.1. I_0 is usually known from a calibration measurement using rays outside the actual field of measurement (FOM), as the attenuation of air is negligible. A typical image matrix size today is 512^2, and thus, a minimum of $512^2 = 262{,}144$ independent projection values are needed. (In CT, any single measurement along a given direction is called a projection. Each projection consists of the sum of the attenuation coefficients of all materials along one ray.) If one tries to solve this problem iteratively, as it was the case in the early days of CT, this would result in a linear equation system of 512^2 equations with 512^2 unknown parameters.

Hence, one soon turns to the more practical approach of filtered back projection (FBP). This numerical approach is still the standard today and is the basis for CT reconstruction algorithms used in all scanners. As the name implies, a filter or convolution kernel is applied in the process, which determines the image characteristics by balancing resolution and noise. For example, "sharp"

kernels increase resolution and noise, whereas "soft" kernels decrease them. Resolution and noise are therefore inherently linked for such reconstruction approaches.

For practical purposes, the value displayed in CT images is not the attenuation coefficient itself but the so-called CT value or CT number (CT#), which is given in Hounsfield unit (HU). It is defined as

$$\text{CT\#} = \left[\frac{(\mu - \mu_{\text{water}})}{\mu_{\text{water}}}\right] \times 1000 \text{ HU} \qquad (1.2)$$

where μ_{water} is the attenuation coefficient of water. The reason for introducing the CT value lies in the fact that the attenuation coefficient is a rather inconvenient measure, as it depends on the x-ray spectrum used. It immediately follows that μ_{water} in Equation 1.2 is specific for the selected tube voltage and needs to be determined by calibration measurements for each voltage setting available. From Equation 1.2, it is also clear that the CT value of water is 0 for any given measurement and that of air (with negligible, meaning no, attenuation) is –1000 HU.

The typical x-ray spectrum used in CT imaging, however, is a polychromatic one. Hence, the spectrum changes as photons are attenuated on the x-ray's path through the material and the assumption of a monoenergetic mean energy in Equation 1.1 is violated. This effect is usually ignored in initial image reconstruction for all materials except water and results in beam hardening artifacts.

A more detailed overview of CT systems and image reconstruction techniques may be found in works by Flohr et al. [13,14].

1.2.1 Technology

The basic components of a CT system include the gantry, the x-ray source or tube, a high-powered generator, detector and detector electronics, data transmission systems (slip rings), and a computer system for image reconstruction and manipulation. The overall performance depends on each one of these key components.

Today's CT scanners use the so-called "rotate/rotate" geometry, where the x-ray tube and the detector are mounted onto a gantry that rotates around the patient. The detector arc typically contains 700 or more detector elements, which cover a FOM of usually 50–70 cm. For multislice systems, several such detector rows exist. The x-ray attenuation of the object is measured for each individual detector element. The measurements acquired at the same angular position of the system form a projection or view. Typically, 1000 projections are measured during a full rotation.

With rotation times in the millisecond range, the gantry has to withstand high gravitational forces (~28 G for 0.33 second rotation time). Of particular importance is the stability of the focal spot associated with the generation of x-rays as well as the corresponding detector position to ensure the high precision of measurements and eventually image resolution in the submillimeter domain. However, rotation times of less than 0.25 second (mechanical forces > 45 G) appear to be beyond today's mechanical limits.

With fast data acquisition times, today's x-ray tube/generator combinations are required to deliver peak power in the range of 60–100 kW. The typical x-ray spectra available in CT imaging today use a range of user-selectable voltage settings, usually in discrete steps ranging from 70 to 150 kV. As a typical example, systems might offer four settings at 80, 100, 120, and 140 kV. The range is due to different requirements by different clinical applications for optimal image quality and/or best possible signal-to-noise ratio at lowest dose. A conventional tube design includes an anode plate of typically 160–220 mm diameter that rotates in a vacuum housing. A cathode-generated electron beam is accelerated in vacuum toward the anode, and on hitting the anode the kinetic energy of the electrons is transformed into heat and x-ray photons. The resolution of the system depends on the size and stability of the focal spot at the anode. Typical dimensions are nominal sizes of 1.0–1.2 mm (large) and 0.3–0.6 mm (small) focal spots. The anode in most (diagnostic) x-ray tubes consists mainly of tungsten, mostly because of its high atomic number ($Z = 74$) and extremely high melting point, both required for efficient x-ray production and heat resistance, respectively. The heat storage capacity of the tube, hence, determines the performance level: the bigger the anode plate, the larger the heat storage capacity and the more scan seconds delivered until the anode plate reaches its temperature limit. An alternative design is the rotating envelope tube [15], where the anode plate constitutes an outer wall of the rotating tube housing. Efficient anode cooling via thermal conduction occurs owing to direct contact with the cooling oil. A permanent electromagnetic deflection of the electron beam is needed to position and shape the focal spot on the anode due to the central rotating cathode. This is also used for the double *z*-sampling technology mentioned earlier [13].

All state-of-the-art CT systems use solid-state detectors. Materials currently in use have comparable performance ensuring efficient x-ray detection. Suitable detector materials have a high atomic number and short afterglow time to enable the fast gantry rotation speeds and data acquisition. Typical materials are cadmium tungstate, gadolinium oxide, or gadolinium oxisulfide with suitable dopings. In course of the measurement, the absorbed x-rays are converted into visible light, which is then detected by a photodiode. The resulting electrical current is amplified and converted into a digital signal.

1.2.2 Data Rates and Data Transmission

With increasing number of detector rows and decreasing gantry rotation times, the data transmission systems of multislice CT scanners must be capable of handling significant data rates. With a typical 64-slice CT system, data rates of 180–200 MB/s are reached. This constitutes a challenge both for data transmission off the gantry and for subsequent image reconstruction systems, in particular, if real-time data processing is required. Contactless transmission technology is the state of the art used for data transfer, either laser transmission or electromagnetic transmission with a coupling between a rotating transmission ring antenna and a stationary receiving antenna. In image reconstruction, images are reconstructed at a rate of up to 40 images per second for a 512 × 512 matrix.

1.3 Scan Modes and Scan Parameters

The two basic modes of CT data acquisition are sequential (axial) and spiral (helical) scanning.

1.3.1 Sequential (Axial) Scanning

In sequential or axial scanning, a given scan volume is covered in a so-called "step-and-shoot" mode. Data are acquired during a full rotation and the patient table is moved between two individual acquisitions to a new z-position. A detailed theoretical description of the performance of sequential scan modes can be found in work by Hsieh [16]. As a key characteristic, the number of images acquired during a sequential scan corresponds to that of active detector slices. By combining detector signals of the adjacent sections during image reconstruction, the number of images per scan can be reduced and the image slice width can be increased. As an example, a scan with 4 × 1 mm collimation can be viewed at four images with 1 mm slice width, two images with 2 mm slice width, or alternatively one single image with 4 mm slice width. Realizing a thicker slice width by summation of several thin sections is beneficial for examinations that require, on the one hand, narrow collimation to avoid partial volume artifacts and, on the other hand, low image noise to detect low contrast details, such as examinations of the posterior fossa of the skull or the cervical spine.

With the advent of multislice CT, sequential scanning is used only for a few clinical applications, such as head CT, high-spatial-resolution lung CT, perfusion CT, and interventional applications. Recently, the technique experienced a revival in cardiac scanning.

1.3.2 Spiral (Helical) Scanning

Spiral or helical scanning is characterized by continuous gantry rotation and continuous data acquisition while the patient table moves at a constant speed (Figure 1.3). With multislice CT systems, it has become the method of choice for most applications. A main difference to sequential CT and at the same time a significant advantage is the possibility of freely and retrospectively choosing image positions and reconstruction increments. While in sequential CT, scan and image position are directly coupled, this restriction is no longer valid in spiral CT.

1.3.3 Pitch

An important parameter to characterize a spiral scan is the pitch p. According to International Electrotechnical Commission specifications (IEC 60601-2-44 Amd.1), the pitch p is given by table feed per rotation divided by the total width of the collimated beam. The pitch illustrates whether data acquisition occurs with gaps ($p > 1$) or with overlap ($p < 1$) in the longitudinal scan direction. For general radiology applications, clinically useful pitch values range from 0.5 to 2. Exceptions occur in the special case of electrocardiogram (ECG)-gated cardiac scanning, where very low pitch values of 0.2–0.4 are applied to ensure gapless volume coverage of the heart during each phase of the cardiac cycle, and in high-pitch scanning with DSCT systems, where pitch values as high as 3.4 can be used.

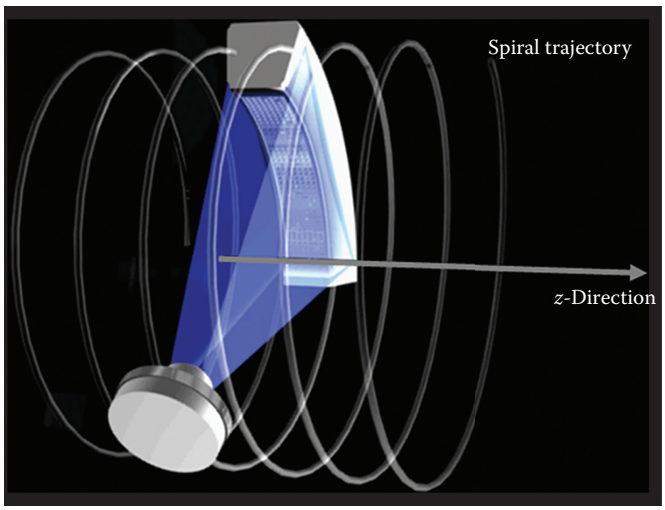

FIGURE 1.3
Principle of spiral (helical) CT scanning: the patient table moves continuously through the gantry while data are acquired during multiple rotations. Thus, the path of the x-ray tube and detector relative to the patient corresponds to a helix. To reconstruct an image at a specified image position, data needs to be interpolated in the z-direction to estimate a complete CT dataset at that position.

1.3.4 Collimated and Effective Slice Width

The continuous data acquisition during table movement results in a helical trajectory of the measured data points. Although the actual image reconstruction is, in principle, the same as in sequential CT, an additional interpolation step is required to reconstruct an image at a specified *z*-position. This interpolation in the longitudinal direction is used to generate a consistent planar dataset from the spiral data for an arbitrary image position.

The basic interpolation algorithms used are the 180-MLI and 360-MLI (multislice linear interpolation) approaches [17,18] or *z*-filter techniques [19]. In a *z*-filter reconstruction, all direct and complementary rays (i.e., rays in the same direction acquired half a rotation earlier or later) within a selectable distance from the image plane contribute to the image. Images with different slice widths can be retrospectively reconstructed from the same CT raw data by adjusting this distance and the corresponding weighting functions. Hence, *z*-filtering allows the user to trade off *z*-axis resolution with image noise (which directly correlates with required dose).

In spiral CT, the slice profile changes to a more bell-shaped curve as opposed to the trapezoidal shape in axial scanning. Interpolation algorithms determine the effective slice width, which now determines *z*-axis resolution as opposed to the collimated beam width in axial scanning.

1.3.5 Cone-Beam Problem in Multislice CT

Modified reconstruction approaches that account for the cone-beam geometry of measured rays are required for CT scanners with 16 or more slices. Here, the individual "fan beams" are tilted by the cone angle with respect to a plane perpendicular to the *z*-axis. The cone angle is largest for the slices at the outer edges of the detector, and it increases with increasing number of detector rows (assuming their width is kept constant). Of the introduced reconstruction approaches, an option is the 3D FBP reconstruction. Here, one accounts for the cone-beam geometry by back projecting the individual projections into a 3D volume along the lines of measurement [20]. An alternative reconstruction approach is to split the 3D reconstruction task into a series of conventional 2D reconstructions, each of them on tilted intermediate image planes. One such implementation is the adaptive multiple plane reconstruction [21].

Regardless of the specific reconstruction algorithm used, narrow collimation scanning is generally recommended. Even if the pitch has to be increased for equivalent volume coverage, partial volume artifacts can be better suppressed when data are acquired at narrow collimations. Hence, just like in single-slice spiral CT narrow collimation scanning is the key to reduce artifacts and to improve image quality.

1.3.6 Double *z*-Sampling

As a means to improve spatial resolution in the longitudinal direction, the concept of double *z*-sampling was introduced in 2003 [13]. By continuous electromagnetic deflection of an electron beam in a rotating envelope x-ray tube, the focal spot is alternated between two different positions on the anode plate, improving data sampling along the *z*-axis. Two subsequent readings are shifted by half a collimated slice width in the patient's longitudinal direction. As a consequence, spatial resolution in the longitudinal direction is increased. The first system using this technology, a 64–multi-detector CT (MDCT) system (Somatom Sensation 64; Siemens, Germany), combined two 32-slice readings to one 64-slice projection with a sampling distance of 0.3 mm at the isocenter (Figure 1.4). Thus, objects that are less than 0.4 mm in diameter can be routinely resolved at any pitch. Last but not least, a further benefit of double *z*-sampling lies in the suppression of spiral "windmill" artifacts.

1.3.7 Special Considerations: Cardiovascular CT

Imaging of the heart was enabled by ECG-synchronized data acquisition. Feasibility was proved with four-slice CT systems; using optimized image reconstruction techniques, a temporal resolution of ≤250 ms could be achieved with 0.5 second of gantry rotation time. This proved sufficient for adequate visualization of the coronary arteries at low heart rates [10].

However, it required the technological advances implemented in 64-slice scanners to potentially provide sufficient robustness for a successful integration of coronary CTA into routine clinical algorithms [22]. Temporal resolution is significantly improved because of the reduction of gantry rotation times to 0.33 second,

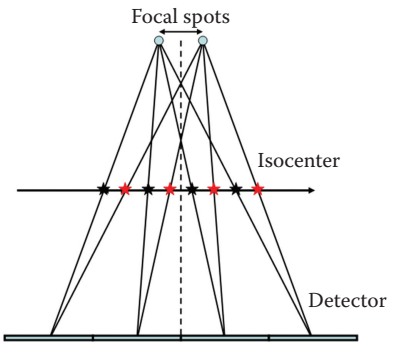

FIGURE 1.4
z-Flying focal spot technique: the electron beam is electromagnetically deflected between two positions on the anode plate. Two subsequent measurements shifted by half the collimated slice width at the isocenter can be combined, thus performing 64-slice acquisition with 32 detector element rows.

whereas increased volume coverage at submillimeter collimation enables high-resolution imaging of the coronary arteries. Today high-end single-source scanners offer rotation times as low as 0.27 second and can acquire up to 320 slices with an isotropic submillimeter resolution.

For ECG-synchronized examinations of the heart, either ECG-triggered sequential scanning or ECG-gated spiral scanning can be used. In ECG-triggered sequential scanning, the heart is covered by subsequent sequential scans in a step-and-shoot technique. In between the individual scans, the table moves to the next *z*-position. Owing to the time necessary for table motion, typically every second heartbeat is used for data acquisition (Figure 1.5).

With retrospective ECG gating, the heart is covered continuously in a spiral scan. The patient's ECG signal is recorded simultaneously to data acquisition to allow for a retrospective selection of the data segments used for image reconstruction. Only scan data acquired in a predefined cardiac phase, usually the diastolic phase, are used for image reconstruction. The data segments contributing to an image start with a user-defined offset relative to the onset of the R waves, similar to ECG-triggered axial scanning (Figure 1.6).

Temporal resolution is one key parameter in cardiac CT imaging. In a single-segment reconstruction, consecutive data from the same heart period are used to generate an image. At low heart rates, a single-segment reconstruction yields the best compromise between temporal resolution and volume coverage with thin slices. Temporal resolution can be improved by using scan data of subsequent heart cycles for image formation in a multisegment reconstruction. With increased number of segments higher temporal resolution is achieved but at the expense of slower volume coverage. Additionally, depending on the relationship between the rotation time and the patient's heart rate, temporal resolution is generally not constant: there are "sweet spots," heart rates with optimal temporal resolution and heart rates for which temporal resolution cannot be improved beyond half the gantry rotation time. Multisegment approaches rely on complete periodicity of heart motion, and they have limitations in patients with arrhythmia or patients with changing heart rates. In general, the reliability of obtaining good image quality with multisegment reconstruction decreases with increasing number of segments.

1.4 New Developments and Advances in CT

The technical advances in MDCT have been accompanied by a substantial enhancement of the clinical potential of CT. It seems, however, that adding even more detector rows will no longer directly translate

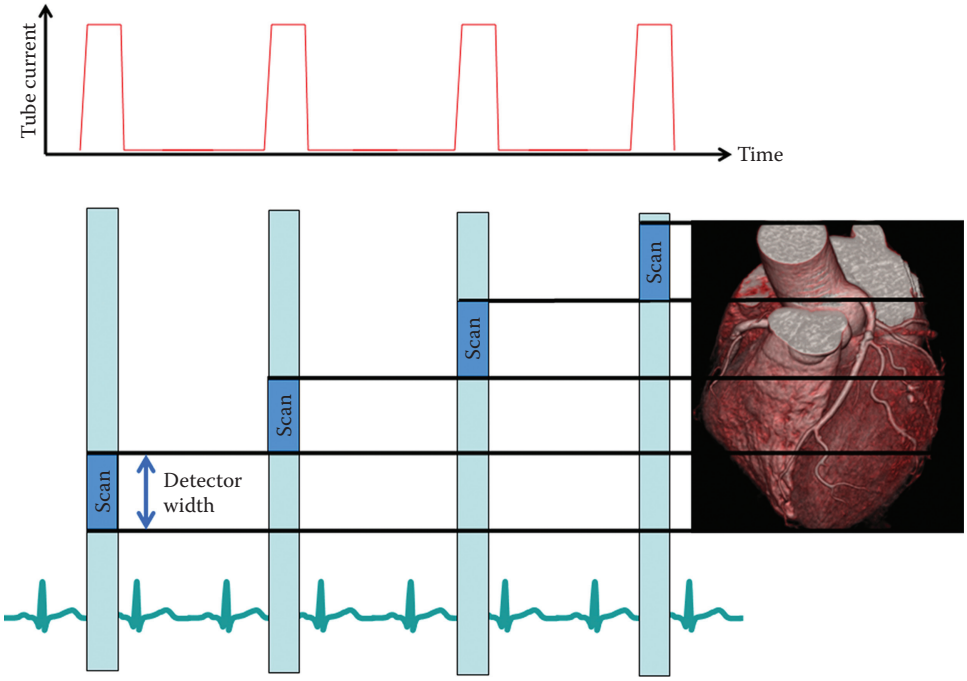

FIGURE 1.5
Axial or step-and-shoot mode: a series of axial scans at different *z*-positions is performed at a predefined temporal offset from the R wave. Every second RR interval is used for table movement.

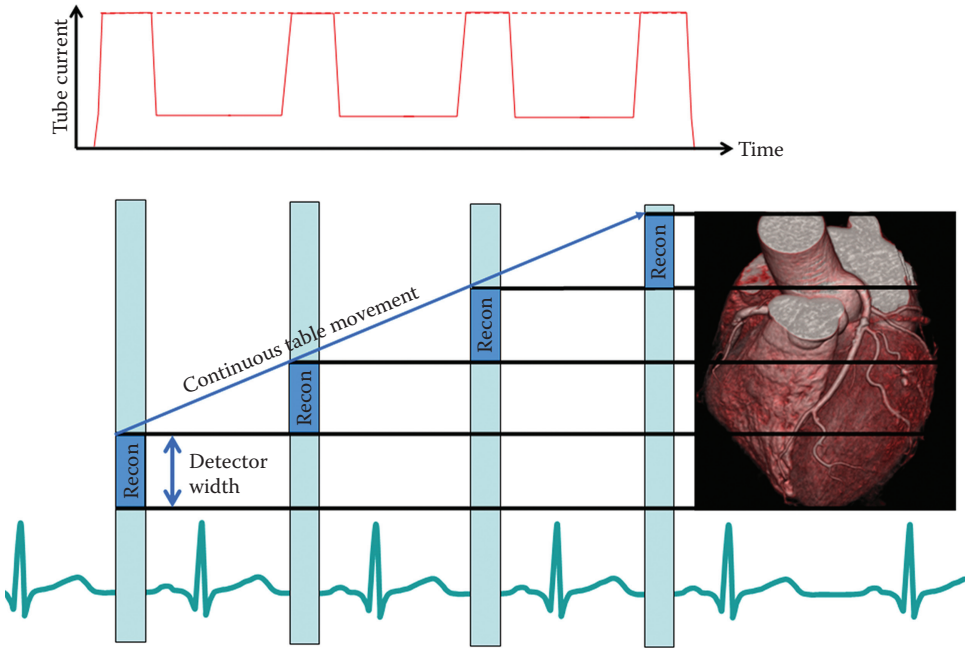

FIGURE 1.6
Electrocardiogram (ECG)-gated spiral scanning: as the table moves continuously at a low pitch, continuous spiral scan data of the heart are acquired. The patient's ECG signal is recorded as a function of time and is used to retrospectively identify scan data acquired in a defined cardiac phase to be used for image reconstruction. Tube current can be kept constant (dotted line) over the cardiac cycle or decreased during those phases that are not used for image reconstruction (solid line) to reduce dose.

into clinical benefit. Hence, recent advances in CT have focused on remaining limitations such as insufficient temporal resolution for cardiac CT or limited scan range to dynamic examinations of entire organs. Scanners with large area detectors and DSCT systems represent the two-system concepts at the moment.

1.4.1 CT Systems with Area Detector

The first commercially available system with an area detector was introduced in 2007. It consisted of a scanner with 320 × 0.5 mm collimation and 0.35 second gantry rotation time. CT scanners with area detectors are optimized for the acquisition of sequential scan data covering entire organs, such as the heart [23], the kidneys, or the brain [24] with zero table feed. The resulting reconstructed scan volume is cone shaped. Hence, with a detector collimation of 320 × 0.5 mm a coverage of 16 cm in the longitudinal direction is feasible at the isocenter, whereas coverage is 11.7 cm at a distance of 160 mm from the isocenter. By appending axial scans shifted in the z-direction, also called "stitching," larger scan volumes in the z-direction can be covered at the expense of overlap scanning. Single-step cardiac CTA and dynamic or perfusion CT are good indications for this technology [23,25,26].

Increased x-ray scatter due to larger detector z-coverage, however, poses a challenge in particular for perfusion scanning. Scattered radiation may cause hypodense artifacts as well as affect CT-number stability. Ultimately, scatter-induced noise may reduce the contrast-to-noise ratio (CNR) in the images.

1.4.2 DSCT

In DSCT, two acquisition systems are mounted into one gantry with an angular offset of 90°–95° (Figure 1.2). Each acquisition system provides overlapping 0.6 mm slices using z-flying focal spot technique (Figure 1.4). Whereas one system covers the full FOM (FOM = 50 cm in diameter), the other is restricted to a central FOM (26–33 cm). We can acquire 64 or 128 overlapping 0.6 mm slices with double z-sampling, the shortest gantry rotation time being 0.33–0.28 second. DSCT provides higher temporal resolution without the necessity of faster gantry rotation. Generally 180° of scan data is used for image reconstruction in cardiac CT; this can be separated into two 90° data segments that are simultaneously acquired by the two acquisition systems of DSCT systems in the same phase of the patient's cardiac cycle and at the same anatomical level. Therefore, the total data acquisition time per image is reduced to a quarter of the gantry rotation time. For a rotation time of 0.28 second, the resulting temporal resolution is 75 ms, independent of the patient's heart rate.

Sampling gaps that lead to severe image artifacts occur if the pitch is increased beyond $p = 1.5$ in single-source

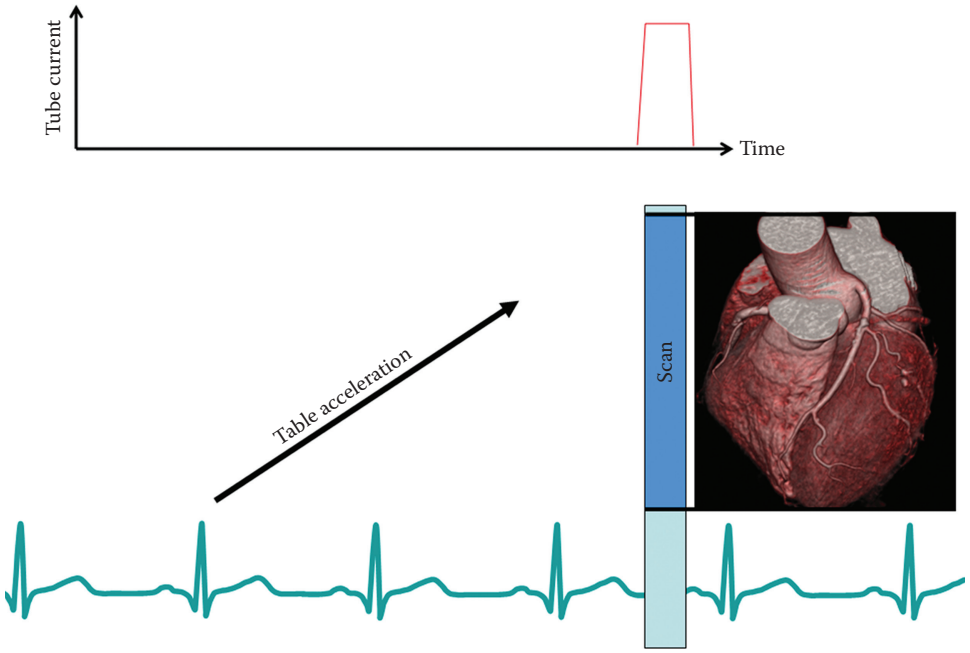

FIGURE 1.7
ECG-triggered high-pitch spiral dual-source CT (DSCT): the patient table is accelerated and reaches the scan volume at a predefined cardiac phase. At this *z*-position, data acquisition is started and the entire heart is covered in a fraction of a heartbeat. The blue box indicates the total scan time, which is typically 0.25–0.27 second. The images are reconstructed at slightly different phases of the cardiac cycle. Each of the images is reconstructed using data of a quarter rotation from each x-ray tube, resulting in a temporal resolution of 75 ms per image.

MDCT. DSCT systems can fill these gaps with data from the second measurement system a quarter rotation later, which allows to increase the pitch up to $p = 3.4$ (Figure 1.7). It is important to notice that no redundant data are acquired, each individual image has a temporal resolution of a quarter of the rotation time, and data acquisition is limited to an FOM of 33 cm in diameter. Scan speeds up to 450 mm/s can be achieved, sufficient to cover the heart in a single heartbeat [27–33]. The patient's ECG is used to trigger both table motion and data acquisition. Standard, that is, non-ECG-gated, scanning uses the high speed for the examination of larger anatomical ranges in very short scan times, for example, when the patient has limited ability to cooperate, such as in pediatric radiology [34].

1.4.3 Dual-Energy CT

In DSCT systems, both x-ray tubes can be operated at different tube voltage and current settings, allowing the nearly simultaneous acquisition of DECT data, thus overcoming the limitations of single-source DECT proposed more than 30 years ago [35–37]. DECT proved to be beneficial in a variety of clinical indications, including tissue characterization in abdominal imaging (small indeterminate hepatic or renal lesions, adrenal gland lesions, renal calculi, etc.), cardiovascular imaging (differentiation of iodine and calcium for bone-free CTA, follow-up of patients with endovascular aneurysm repair, etc.), musculoskeletal imaging (calcium or uric acid quantification, calculation of pseudomonochromatic images for metal artifact reduction), and quantification of the local blood volume in contrast-enhanced scans [30–32,38–41].

Nowadays DECT data can also be acquired with high-end single-source CT systems, using either dual-layer detector panels or rapid kV-switching technology. Dual-layer detector systems involve placement of two layers of detector elements on top of each other. The upper detector layer predominantly absorbs lower-energy photons and the second detector layer absorbs higher-energy photons. Although it is not commercially available, this approach suffers disadvantages in that the spectral separation is inferior to dual-energy approaches relying on two different kV settings. With rapid kV-switching techniques used in single-source CT systems, the tube voltage alternates hundreds of times per second between two kV settings during the acquisition. The nearly simultaneous acquisition of both low- and high-energy data avoids registration problems owing to organ motion or contrast agent dynamics. However, the method is restricted to relatively slow rotation times (0.6–1 second) as a sufficient number of projections (>600) need to be acquired at each kV setting. Furthermore, current tube technology allows switching the voltage between consecutive readings, but not the tube current. Hence, a fixed tube current is required—at both low and high kV settings.

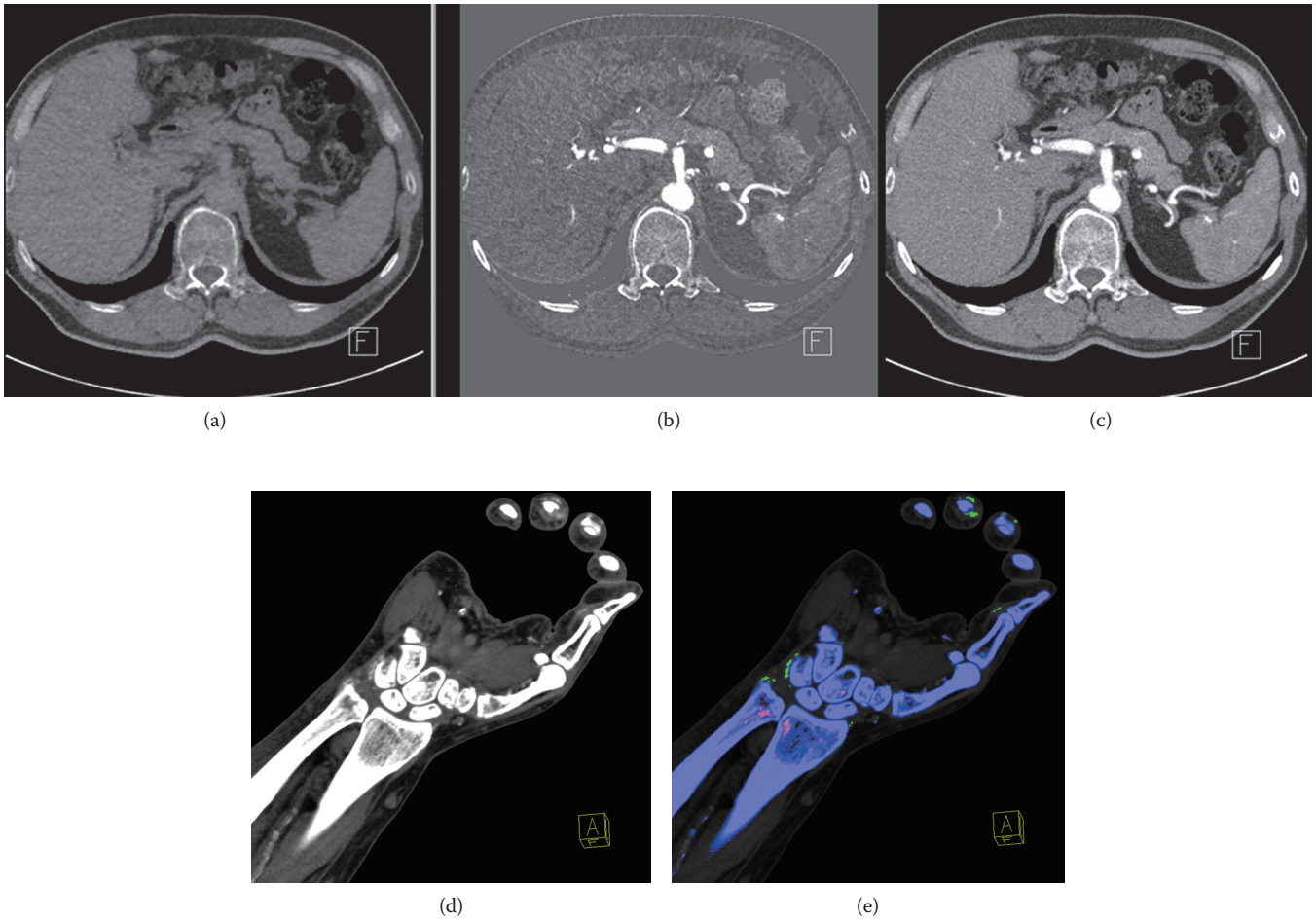

(a) (b) (c)

(d) (e)

FIGURE 1.8
Three different visualizations of contrast-enhanced abdominal CT with dual energy: (a) virtual non-enhanced, (b) iodine map, and (c) combined 120-kV-equivalent contrast-enhanced CT. (d) Patient with a history of gout. (e) Differentiation of calcium (blue) and urate (green) deposition on color-coded DECT image.

DECT can obtain information on the chemical composition of tissue based on differences in the photoabsorption process; the dominant attenuation process at low photon energies; and Compton scattering, dominating at higher photon energies. Photoabsorption is very weak for hydrogen, but strong for iodine/contrast material. The relative strength of photoabsorption with respect to Compton scattering can be determined by DECT. Data analysis is based on material decomposition (Figure 1.8).

1.4.4 Iterative Reconstruction Algorithms

As mentioned in Section 1.2, FBP is a practical and efficient approach to image reconstruction, where spatial resolution is directly correlated with increased image noise. Iterative reconstruction techniques, well established in positron emission tomography (PET) and single photon emission CT) data reconstruction, have been only recently reinvigorated in CT as a method to improve image quality, enhance image resolution, and lower image noise [42].

A decisive benefit of iterative reconstruction constitutes the ability to decouple spatial resolution and image noise to a certain degree. In general, a correction loop is introduced in the image reconstruction process. After an initial image has been reconstructed from the measured projection data, synthetic projections are calculated that exactly represent the reconstructed image. The deviation between measured and calculated projections is used to reconstruct a correction image and refresh the original image in an iterative loop. Each time the image is updated, nonlinear image-processing algorithms are used to stabilize the solution. They maintain or enhance spatial resolution at higher object contrasts and reduce image noise in low-contrast areas. The repeated calculation of corrections reduces image artifacts, and image resolution can be increased by carefully modeling the measurement system during forward projection in a model-based iterative reconstruction [42].

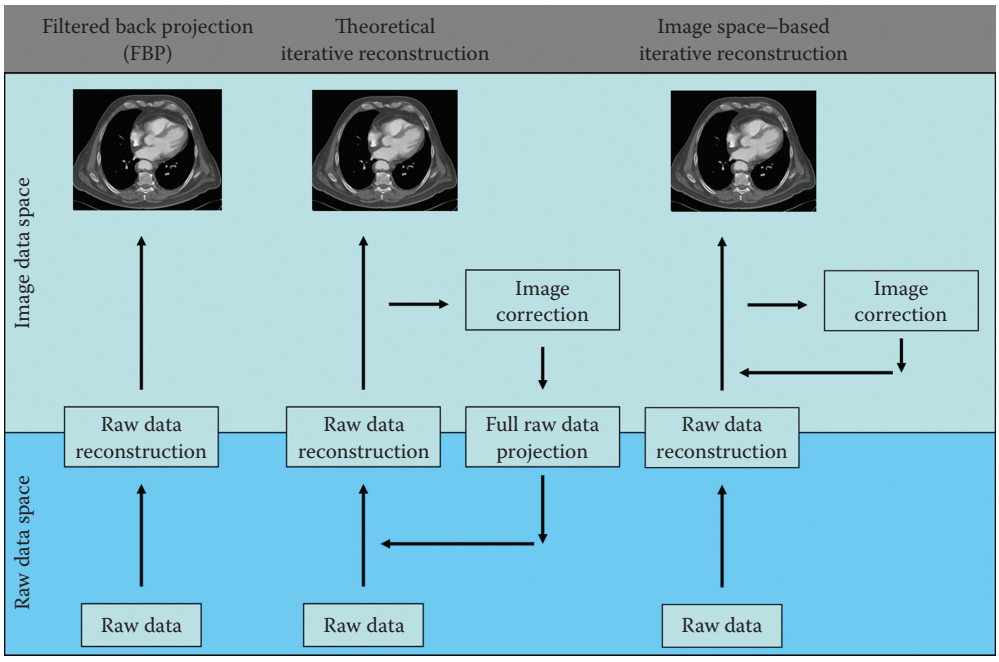

FIGURE 1.9
Image reconstruction: iterative correction loops are introduced to reduce noise and artifacts. Theoretical iterative reconstruction most accurately improves image quality but is computationally demanding. Image space-based iterative reconstruction skips the full raw data projection in the correction loop and is computationally less demanding. Variants and combinations of these techniques have been introduced in multi-detector CT (MDCT) reconstruction software.

In the meantime, several implementations of iterative reconstruction methods have been introduced commercially by the major vendors (Figure 1.9).

1.5 Radiation Dose Reduction

With CT being the imaging modality of choice in many situations, radiation exposure is of concern for both patients and physicians. To reduce the dose for an individual examination, the most important principle after critical review of the indication is to adhere to ALARA (as low as reasonably achievable). Besides adjusting the techniques to the diagnostic question, one can make use of many different techniques to reduce radiation exposure.

1.5.1 Tube Current Reduction

The most important lever to reduce radiation exposure is to adapt dose to the patient size and weight [43,44]. This is of particular importance in pediatric imaging. Not only patient habitus but also the imaging study itself has impact on radiation exposure: imaging the liver requires less noise—and therefore higher radiation exposure—to detect and differentiate small lesions, as compared to imaging the lung. More noise can be accepted in imaging the paranasal sinuses in the evaluation of sinusitis as compared to tumor staging. The acceptable level of noise is difficult to determine and is user dependent. Iterative reconstruction techniques compensate for higher noise to allow dose reduction of 50% in abdominal [45] and 25%–80% in chest CT [46–49].

1.5.2 Anatomical Tube Current Modulation

More straightforward than manually selecting patient-individual tube current settings by adjusting the x-ray tube current are techniques that use automatic anatomical tube current modulation (automatic exposure control [AEC]). AEC modifies the tube output in the through-plane (z-axis) direction to maintain adequate dose when scanning body regions with different attenuation, for instance, chest and abdomen. In addition, angular tube current modulation can be performed during each rotation of the gantry to compensate for strongly varying x-ray attenuations in asymmetrical body regions such as the shoulders and pelvis. The variation of the tube output is either predefined by analysis of the localizer scan (topogram, scout view) or determined online by evaluating the signal of a detector row online. In practice, a reference (either reference exposure or other types of image quality metrics) is selected, which will be applied if the patient's attenuation matches the stored standard reference. If the patient's attenuation deviates, the tube output will be adapted accordingly (Figure 1.10). Some

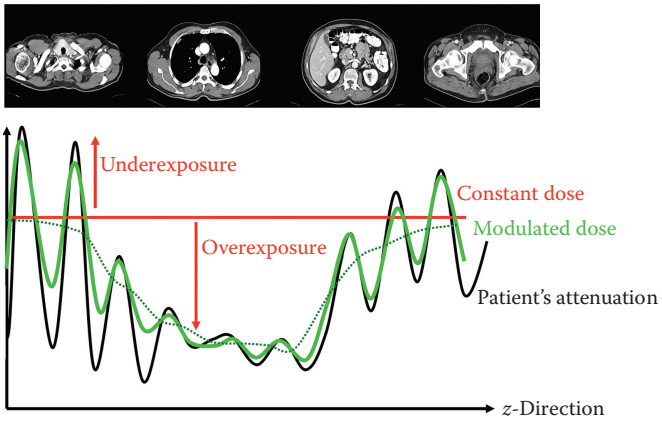

FIGURE 1.10
Anatomical dose modulation: with constant tube current, the thoracic inlet and the pelvis are underexposed, whereas the thorax and the abdomen are overexposed. Adapting the radiation dose to a patient's attenuation can be achieved by the online modulation of tube current, ensuring consistent image quality throughout the scan volume.

algorithms try to adapt the tube current such as to maintain constant image noise in all examined body parts, whereas others allow for a weaker increase of the tube current with increasing body size, trying to match the radiologist's perception. The potential for dose reduction is significant with the use of anatomical dose modulation approaches; values of 20%–68% without degrading image quality and depending on the body region have been reported [50–52]. However, the effects of AEC are limited with larger detector *z*-coverage, because the detector can cover different anatomical regions (i.e., transition from liver to lung or from shoulder to neck), each requiring individual tube current settings.

A variant of automatic anatomical tube current modulation designed to specifically reduce radiation exposure to selected organs is the organ-based tube current modulation. Thus, radiation exposure can be reduced for targeted organs such as eye lenses or the female breast. Therefore, the x-ray tube current is reduced in a selectable angular range, for example, when the x-ray tube moves directly in front of the female breast. The tube current has to be correspondingly increased when the x-ray tube is on the opposite side, to maintain image quality. Overall radiation dose is not reduced in this case, but distributed differently in the scan plane. Local radiation dose to the breast or to the thyroid gland can be reduced by 20%–35% without loss of image quality [53].

1.5.3 Adaptation of the X-Ray Tube Voltage

Not only the tube current, but also tube voltage may be adapted to patient size for further reduction of radiation exposure. Decreased tube voltage results in reduced dose and higher image noise, but attenuation values of iodine are also significantly higher. As a consequence, a specified CNR considered adequate for diagnosis can be reached by using lower tube voltage settings, especially in CTA. Since tube voltage is not linear to dose, in clinical practice it will not simply suffice to change tube voltage settings; rather, a simultaneous adjustment of tube current is required. It is therefore difficult to manually adjust parameters, and tube voltage adjustment has rarely been used routinely. Approaches to select tube voltage and adapt tube current automatically, using information on the patient's attenuation from the localizer scan, and accounting for the planned examination type (e.g., nonenhanced scan, contrast-enhanced parenchymal scan, and CTA) and system limitations (e.g., maximum tube current), are needed to translate this technology into everyday use. Depending on the examination type, dose reduction between 10% and 30% is possible [54,55].

1.5.4 ECG-Gated Dose Modulation for Cardiac Spiral CT

In spiral acquisition mode, data are acquired continuously over multiple heart phases while the patient's table moves at low pitch values. Although it thus provides the ability to retrospectively select the phase of the cardiac cycle during which images are reconstructed, and to maximize image quality, the penalty is increased radiation exposure. Dose reduction is facilitated through ECG-pulsing techniques, where tube current is modulated during the complete spiral CT scan: the tube current is maintained at 100% of the desired level only during a predefined phase of interest of the heart cycle. During the rest of the time the current is substantially reduced. This method is based on the continuous monitoring of the ECG and an algorithm that predicts when the desired ECG phase will start (Figure 1.6).

1.5.5 ECG-Triggered CT

ECG-triggered sequential CT, also known as step-and-shoot mode, is the recommended acquisition mode [56]. It is a very dose-efficient way of ECG-synchronized scanning because only the very minimum of scan data needed for image reconstruction is acquired during the previously selected heart phase (Figure 1.5). The patient's ECG signal is monitored during examination, and axial scans are started with a predefined temporal offset relative to the R waves. Although advanced algorithms can detect extrasystoles and skip them for data acquisition (Figure 1.11), the method reaches its limitations in patients with severe arrhythmia, since ECG-triggered axial scanning depends on a reliable prediction of the patient's next cardiac cycle by using the mean length of the preceding cardiac cycles.

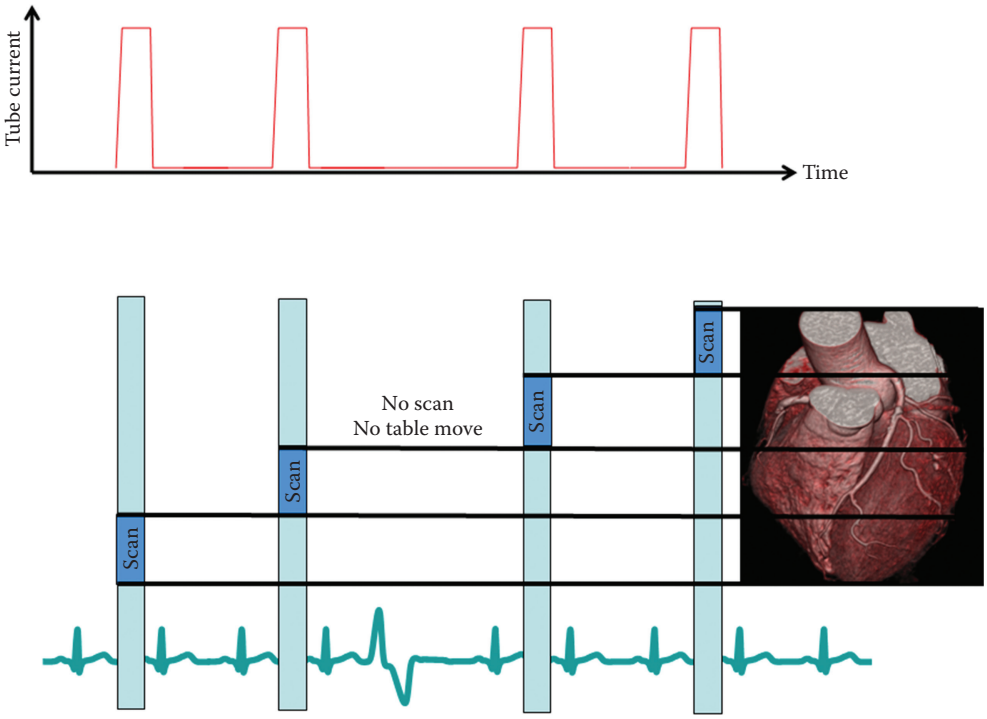

FIGURE 1.11
Axial scanning depends on a regular and predictable heart rate; advanced algorithms additionally allow flexible reaction to arrhythmia occurring during the scan.

A dedicated low-dose cardiac scanning mode is available on DSCT systems. Using fast scan speed (pitch values of up to 3.4 in combination with large detector coverage and fast gantry rotation), the heart can be scanned within 250–270 ms in ECG-triggered (high-pitch) spiral mode. No redundant data are acquired; thus, dose is reduced to a minimum [57]. Image quality depends on a low and regular heart rate to precisely predict the optimal scan start.

1.5.6 Dynamically Adjustable Collimation

Spiral CT reconstruction algorithms require scan data beyond the user-defined scan boundaries in the *z*-direction (through-plane direction). This is known as overranging. Over-ranging depends on the detector width and pitch value; with increasing number of slices, broader detectors, and higher pitch, overranging can contribute considerably to a patient's exposure. To reduce radiation exposure from overranging, dynamically adjustable prepatient collimators that allow independent control of both tube collimator blades have been introduced. The collimator blades open and close asymmetrically at the beginning and at the end of each spiral scan. Estimated reductions in effective dose were 16% for the head, 10% for the chest and liver, 6% for the abdomen and pelvis, and 4% and 55% for coronary CTA at pitch values of 0.2 and 3.4 [58,59].

1.6 Contrast Delivery and Safety

CT examinations can be divided into nonenhanced and contrast-enhanced studies. Contrast-enhanced studies may be angiography type (CTA-type) or parenchyma type. Whereas for CTA-type studies maximum contrast is warranted in the vessels of interest, parenchyma-type studies aim to maximize contrast between specific organs and lesions. The type of study significantly influences both contrast material application and scanning strategy.

1.6.1 Contrast Material

Most modern CT contrast agents for intravenous use are nonionic derivates of a tri-iodinated benzene ring. They are monomers that dissolve but do not dissociate in water (low-osmolar contrast media [LOCM]) or dimers that consist of two benzene rings (iso-osmolar contrast media [IOCM]). LOCM with an iodine concentration of 300 mg I/mL have typical osmolality values of 521–672 mosmol/kg H_2O at 37°C, whereas IOCM with an iodine concentration of 320 mg I/mL have an osmolality value of 290 mosmol/kg H_2O at 37°C. The viscosity values are 4.5–6.3 mPas at 37°C for LOCM and 11.8 mPas at 37°C for IOCM (ACR Manual on Contrast Media, version 7, 2010).

Contrast media (CM) are well tolerated with a low rate of adverse events (0.2%–0.7%) and serious events

occurring in 0.01%–0.02% cases. The actual incidence is difficult to determine because similar symptoms may be caused by concomitant medication, anxiety, or other factors on the one hand and underreporting may occur on the other hand. Side effects are usually classified as mild (nausea, mild vomiting, urticaria, itching), moderate (severe vomiting, marked urticaria, bronchospasm, facial/laryngeal edema, vasovagal attack), and severe (hypotensive shock, cardiac arrest, respiratory arrest, convulsion). Moderate and severe reactions require immediate medical treatment and transfer to the emergency department or intensive care unit. First-line emergency drugs and instruments that should be in the examination suite are oxygen, adrenaline (1:1000), H1-receptor antagonist, atropine, β2-agonist inhaler, i.v. fluids (saline 0.9% or Ringers solution), diazepam, sphygmomanometer, and a bag valve mask (ESUR Guidelines on Contrast Media, version 7.0, 2008). A structured report for adverse event documentation is highly recommended.

For patients at increased risk of CM reaction, alternative imaging modalities without the need of iodinated CM should be considered. A different iodinated CM should be used in patients with previous reactions. Although clinical evidence of the effectiveness of premedication is limited, there is consensus that steroids and H1-antihistamine are the most relevant agents. The administration of steroids less than 4–6 hours before contrast injection seems to be ineffective. Oral administration of steroids is preferable in all patients except those with enteral malabsorption. In our institution, 30 mg prednisolone or 32 mg methylprednisolone is given p.o. 12 hours and 2 hours, and H1- and H2-antihistamine is given i.v. before CM injection in elective patients.

The other issue with CM is contrast-induced nephopathy (CIN). Different definitions of CIN exist; the most common definition is increase of serum creatinine > 25% or 0.5 mg/dL (44 mmol/L) within 3 days after CM injection without other reasons. Patients with estimated glomerular filtration rate (eGFR) less than 60 mL/min/1.73 m^2 (i.a. application) and eGFR less than 45 mL/min/1.73 m^2 (i.v. application), particularly if secondary to diabetic nephropathy, dehydration, congestive heart failure (NYHA 3–4) and low left ventricular ejection fraction, gout, age > 70 years, and concurrent administration of nephrotoxic medication (i.e., NSAR), are at higher risk of CIN. eGFR in men ($eGFR_{(m)}$) is estimated according to the Cockroft formula (140-age [years] × body weight [kg])/(72 × serum kreatinine [mg/dL]). For eGFR in females ($eGFR_{(f)}$), a conversion factor ($eGFR_{(f)} = eGFR_{(m)} \times 0.85$) is introduced to compensate for different muscle mass. Patients at risk should be hydrated (p.o. or i.v.) at least 4–6 hours before and 24 hours after the examination (100 mL NaCl 0.9%/h), LOCM or IOCM should be used, and nephrotoxic concomitant medication should be stopped 24 hours before the examination. High CM volume, repeated CM application, loop diuretics, and mannitol should be avoided.

If contrast-enhanced CT is necessary, because the critical questions cannot be answered with alternative imaging without the need of iodinated CM injection, we propose the following regime:

Elective examinations, in-house patients:

100 mL/h NaCl 0.9% 6–12 hours prior until 12 hours after the examination

Elective examinations, outpatients:

1000 mL fluids p.o. 12 hours prior and 12 hours after the examination and 300 mL/h NaCl 0.9% (i.v.) 2 hours prior to 4 hours after the examination

Emergency:

100 mL/h NaCl 0.9% as soon as possible prior until 6–12 hours after the examination

Serum creatinine levels should be monitored after CM application to monitor any change in renal function.

According to the updated European Society of Urogenital Radiology CM guidelines, the biguanide metformin can be continued in patients with chronic kidney disease (CKD) stages 1 and 2 (eGFR ≥ 60 mL/min/1.73 m^2) and also in patients with CKD 3 and eGFR greater than or equal to 45 mL/min/1.73 m^2 and i.v. CM injection, all other should stop metformin 48 hours before and restart metformin 48 hours after CM if renal function has not deteriorated. In the emergency situation, metformin should be stopped and restarted 48 hours after CM if serum creatinine/eGFR is unchanged from the preimaging level [60].

1.6.2 Contrast Material Injection in CTA

Short scan times require a short and compact CM bolus. To deliver an appropriate amount of iodine injection, rates of 4–6 mL/s are preferable. The utilization of the contrast bolus can be increased if it is followed by a saline bolus. Flushing of the veins also reduces streak artifacts due to beam hardening, especially at the thoracic inlet. With modern MDCT systems scan time is in the order of seconds, depending on the scan range and scanning technique, ranging from about 250–270 ms for high-pitch cardiac CTA [29] to approximately 10–20 seconds for thoracoabdominal CTA. Therefore, the scan time can be much shorter than the contrast injection time. The most important variable is the iodine delivery rate: the higher the iodine delivery rate, the higher the enhancement. If the injection rate is kept constant, higher concentrated CM (i.e., 350–400 mgI/mL) result in higher vascular enhancement and an earlier

enhancement peak [61]. If the injection rate of less concentrated CM (i.e., 300 mgI/mL) is increased to keep the iodine delivery rate constant, the enhancement will be similar [62]. With multiphasic injection protocols it is possible to tailor vascular enhancement pattern to the specific needs [63,64], especially when using older CT systems with longer acquisition times; but with modern scanners this is necessary only in limited indications, for example, CTA of the lower extremities.

1.6.3 Saline Bolus

A significant amount of CM usually is trapped within the venous system. This CM is not only lost for imaging but may also be the source of streak artifacts. "Pushing" the CM bolus with 0.9% NaCl reduces CM bolus dissipation and reduces trapping of highly concentrated CM in the subclavian vein. In coronary CTA some radiologists prefer to clear the right ventricle (RV) to facilitate evaluation of the right coronary artery, whereas others prefer to have mild enhancement to improve morphologic and functional analysis of the RV (Figure 1.12). Up-to-date power injectors, which are a prerequisite for optimal CTA, have two pistons or reservoirs to supply CM and saline; many of them also have the "split-bolus" feature to mix CM and saline (e.g., 20%–30% CM, 70%–80% saline).

1.6.4 Bolus Tracking

Individual contrast timing (bolus tracking or test bolus injection) is mandatory to achieve optimal image quality. To individualize contrast timing, automatic bolus tracking techniques are provided by all vendors. This technique is fast, easy to use, and requires only a single contrast injection. The operator places a region of interest (ROI) within the target vessel and defines a threshold value at which the examination should start. An additional delay between the trigger time and the data acquisition may be necessary for table movement, switching of the scan mode, and patient instruction. The disadvantages of this technique are that a large target vessel for monitoring contrast arrival is required, calcified plaque can interfere with bolus detection, and there is an additional delay for table movement and patient instructions.

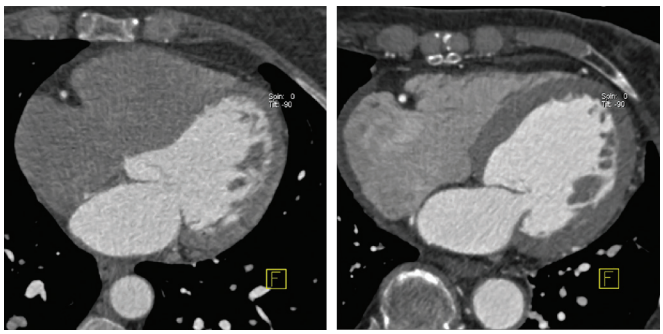

FIGURE 1.12
Saline bolus following contrast media (CM) bolus to "clear" the veins and right ventricle (left); split bolus (20% CM, 80% saline) to differentiate myocardium and blood pool of the right atrium and ventricle.

1.6.5 Test Bolus

Test bolus injection is the alternative to bolus tracking to assess individual circulation time. Again an ROI is positioned in the vessel of interest and a small amount of CM (10–20 mL) followed by a saline bolus is injected. Repetitive low-dose scans without table movement are performed to measure the bolus arrival and peak enhancement. Like with bolus tracking, an empirically determined start delay (i.e., 10–15 seconds for aortic CTA in case of peripheral i.v. line and 5 seconds in case of central i.v. line in a patient with normal cardiac output) can be used for the start of the monitoring scans to reduce radiation exposure. The major advantage of the test bolus technique is that it provides information about the enhancement of both arterial and venous systems. The enhancement peak of the full CM bolus will be later than that of the test bolus [65], but the shape of the test bolus curve, or time-attenuation curve (TAC), can be used to predict the TAC of the full bolus accurately. Furthermore, in organs where venous enhancement may be critical for diagnosis (i.e., carotid artery or renal artery) venous TAC can be determined by placing a second ROI in the vein (Figure 1.13).

Table movement and patient instructions can be performed prior to the optimal image acquisition window, which provides adequate time for the patient to respond. The necessity of an additional injection of CM (10%–20% increase of total amount) is unfavorable.

1.6.6 Parenchymal Imaging

CM delivery and timing is less critical in parenchymal imaging than that in CTA. Flow rates greater than 2.5–3 mL/s do not have a significant effect on organ enhancement [61], and within a wide range of cardiac output a delay of 70 seconds results in sufficient portal venous CM distribution within the liver. Bolus tracking or test bolus techniques can also be used for parenchymal imaging to optimize contrast enhancement, but this is rarely done because of additional radiation exposure and time demand. Most institutions use fixed delays.

1.7 Data Visualization

All modern MDCT systems can be operated in thin-slice collimation mode producing isotropic image data. Often, thin-slice data are reconstructed for visualization

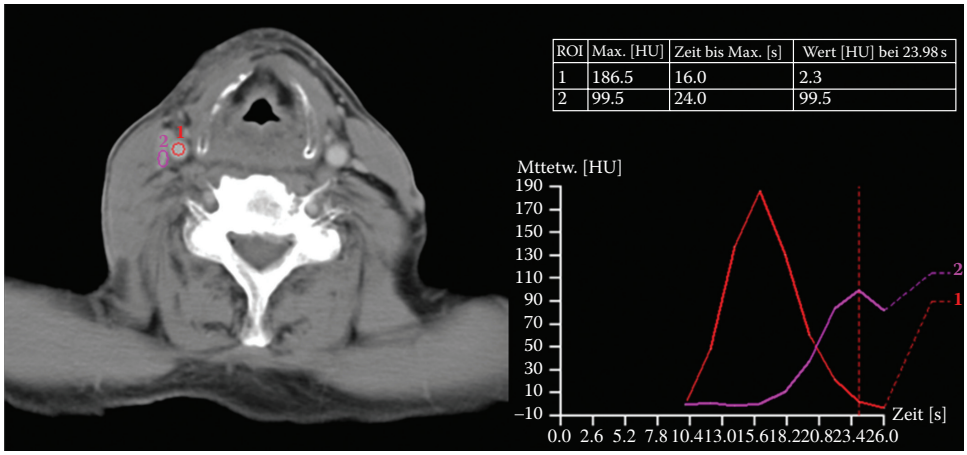

FIGURE 1.13
Test bolus measurement to determine contrast arrival time in common carotid artery and internal jugular vein for optimizing scan delay.

on 3D server–client systems and thick slices for standard image interpretation and image distribution throughout the hospitals. To optimize longitudinal (or *z*-axis) resolution, overlapping image reconstruction should be performed. The reconstruction increment (RI) can be arbitrarily chosen, independent of detector collimation, and 75% of slice width may be a good compromise. The RI denotes the spatial (or temporal) relation of two adjacent images. In-plane spatial resolution is influenced by the reconstruction algorithm or convolution kernel; soft kernels reduce image noise, allow for smooth surfaces with rendering techniques, and improve the perception of low-contrast objects. Sharper kernels improve edge definition, reduce blooming effects, and improve the perception of high-contrast objects at the expense of higher image noise. Image reconstruction is usually performed with a 512^2 matrix, the image matrix, and the reconstructed field of view (FOV) determines the pixel size. The third dimension is determined by the RI. Image matrix, FOV, and RI therefore define the voxel size, which must not be confounded with spatial resolution. The spatial resolution is mainly determined by the CT system geometry, detector aperture, and convolution kernel. Typical spatial resolution is 8–12 lp/cm, which corresponds to an object size of 0.4–0.6 mm [12] with soft tissue kernels; dedicated filter grids and sharp kernels can increase the spatial resolution to 20 lp/cm, which corresponds to an object size of 0.25 mm [66].

1.7.1 Image Post-Processing Techniques

Basic 3D tools like interactive multiplanar reformats, (thin) MIPs, and VRTs are widely available on the scanner console and reading stations. Except MPR, all other methods suppress data to a certain level to enhance special image details.

1.7.1.1 MPR

MPR creates views in arbitrary planes without loss of information. Individually adapted image planes are frequently used in cardiovascular and body imaging, as well as in the planning of interventional procedures. No image manipulation is required, but only 2D views are generated. To decrease image noise especially in low-dose CT, the slice thickness of MPR should be increased. MPR is the method of choice for precise measurements and may be combined with another visualization technique to display 3D anatomy.

A variant of MPR is CPR. CPR provides a 2D image that is created by sampling CT volume data along a predefined track. This technique is employed to display tortuous structures, for example, the coronary arteries (Figure 1.14); manual definition of such curved planes is time consuming and error prone, but algorithms that automatically track vessels are becoming widely available and increasingly accurate.

1.7.1.2 MIP

MIP images are created by displaying only the highest attenuation value from the data along a track through a data volume. Full-volume MIP is only rarely used, because soft tissues are not well represented. Thin-slab MIP images, where the slab thickness of data displayed with the MIP algorithm can be individually adapted, are more frequently used, especially in chest imaging for lung nodule detection. MIP is not suitable for the evaluation of stenosis in cases of dense calcification or stents, but a thin-slab MIP can provide an excellent road map of the vessel course for further evaluation with MPR. MIP is also not ideal to look for intraluminal thrombus or emboli, because the low-attenuating clot may be masked by surrounding contrast material (Figure 1.15).

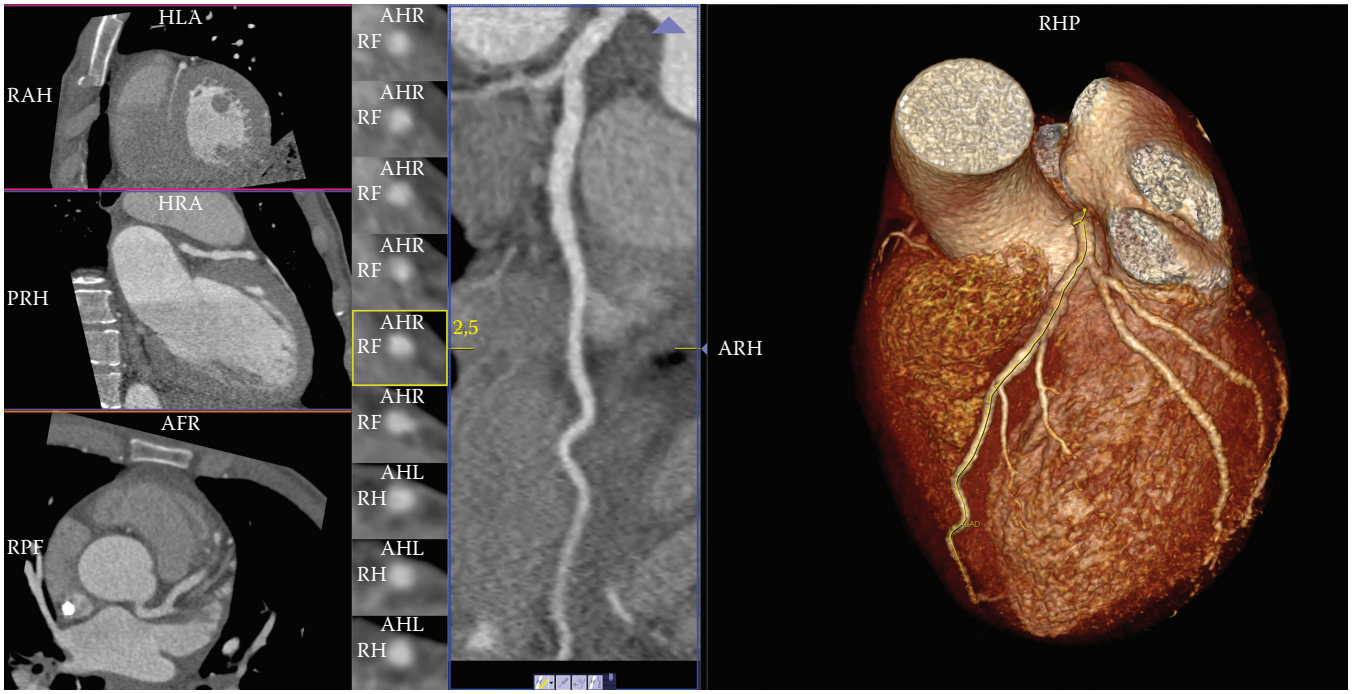

FIGURE 1.14
Visualization techniques: multiplanar reformats (MPR) (left) demonstrates only some parts of tortuous vessels. CPR (middle) displays a complete vessel within one image, and cross-sectional images perpendicular to vessel orientation (left to CPR) can be displayed to measure vessel lumen and wall thickness. The centerline of CPR is marked on a volume-rendered image (right).

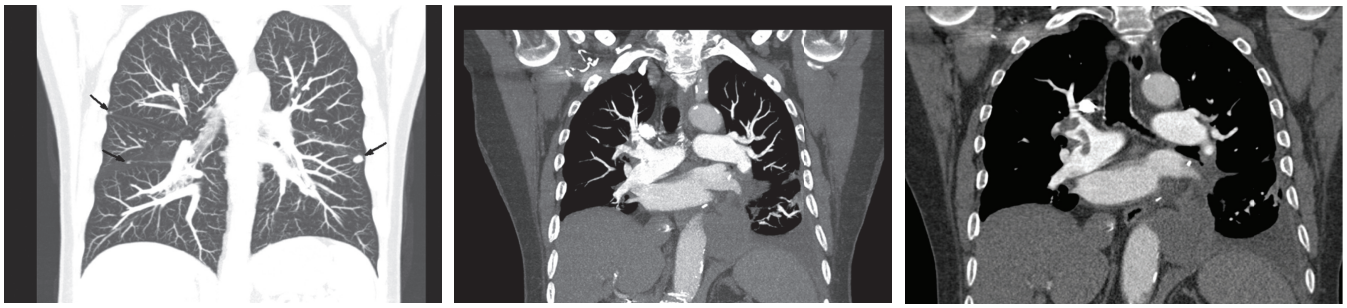

(a) (b) (c)

FIGURE 1.15
Thin maximum intensity projection (MIP): (a) lung nodule detection is enhanced with thin MIP (slab thickness of 10 mm). (b) Patient with pulmonary embolism. Emboli are partly hidden on thin-slab MIP, compared to (c) MPR.

1.7.1.3 Surface Rendering and Volume Rendering

SSD, or surface rendering, is an algorithm that provides a good 3D impression of the surface of an object. In a first step the surface of an object is separated from other structures, usually by thresholding. In a second step, a shading procedure is performed to create light intensity in a given 3D model, simulating surface reflections and shadowing from an artificial light source to enhance depth perception. VRT has supplanted SSD in basically all indications.

VRT is a visualization technique that creates a 3D impression and provides densitometric information. Visualization of CT data is based on transfer functions (TFs) that map measured intensities to colors and opacities [67]. Separation of different tissue types can be performed by applying multiple trapezoids, which can be color encoded, but color is assigned arbitrarily and does not correlate with the linear progression of gray-scale values on conventional CT images. Decreasing the upslope of the trapezoid is comparable to increasing

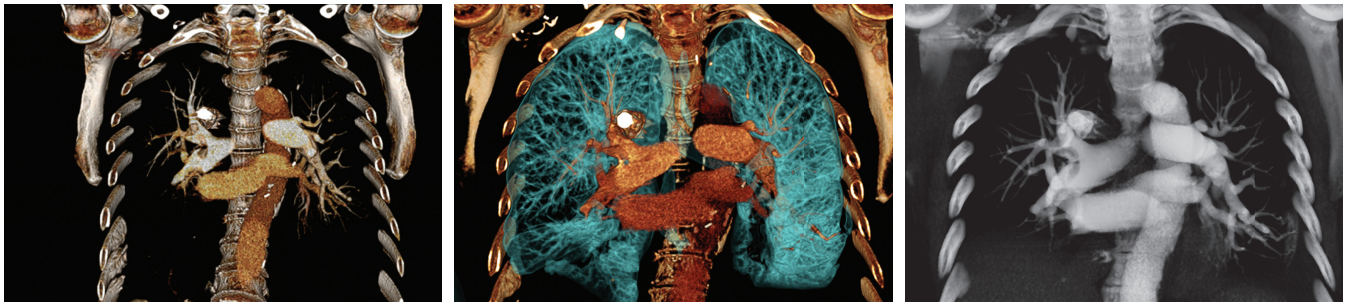

(a) (b) (c)

FIGURE 1.16
Volume rendering: the same patient as in Figure 1.15 is shown. Anatomical structures can be highlighted or suppressed; the depiction of emboli is dependent on parameter settings (a-c: different opacity and trapezoid settings).

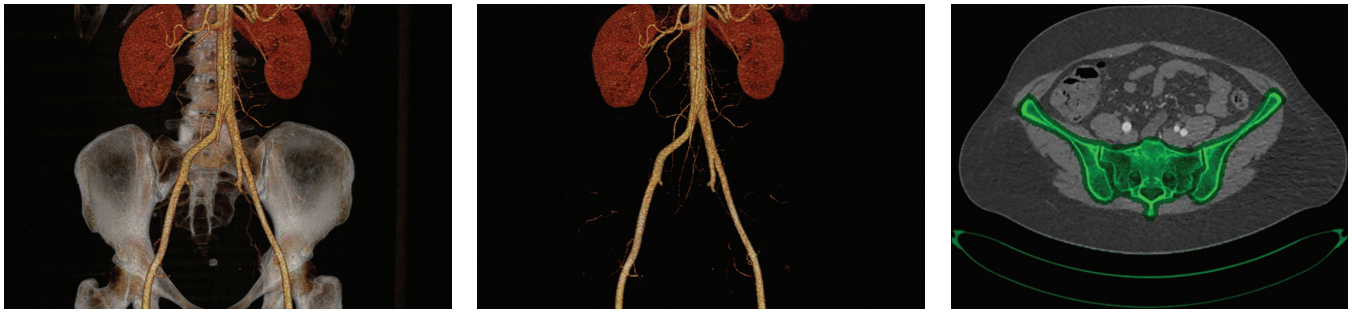

(a) (b) (c)

FIGURE 1.17
Bone segmentation to highlight abdominopelvic arteries: (a) volume rendering (VR), (b) VR without bones, and (c) segmented bone and patient table (green).

the window width on grayscale images. The definition of the trapezoid strongly affects the final image (Figure 1.16).

1.7.1.4 Segmentation

Segmentation can be performed manually or (semi) automatically. Segmentation algorithms are often based on the principle of region growing. Placing one or more seed points initiates the segmentation of the target structure. From these seed points, more and more neighboring voxels that fulfill predefined criteria are included in the segmentation [68]; the segmentation can be optimized using a priori knowledge. To refine the boundary of the segmented structures, morphologic dilation operations may be applied. A particular problem of threshold-based segmentation algorithms are areas with close contact of two tissue types with comparable attenuation, such as bone and contrast-enhanced vessels (Figure 1.17). Segmentation techniques are also used for planning liver surgery and interventional procedures [69–72].

1.7.1.5 Bone Subtraction CTA

For bone subtraction CTA (BSCTA), a nonenhanced CT (NECT) dataset and a contrast-enhanced spiral CT dataset are required. Pixels in the NECT dataset with a CT value above a certain threshold are defined as bone and used to iteratively register the NECT to the CTA dataset. After registration, an initial bone mask is defined in the NECT volume by thresholding. The bone mask is tentatively expanded in three dimensions by morphological dilation, and the bone voxels are set to a HU value of –1024. BSCTA is a robust method of bone elimination, not requiring user interaction (Figure 1.18). Although patient movement between the two scans can be compensated for in cranial CTA, movements can result in incomplete bone or calcification removal in other regions unless additional registration steps or

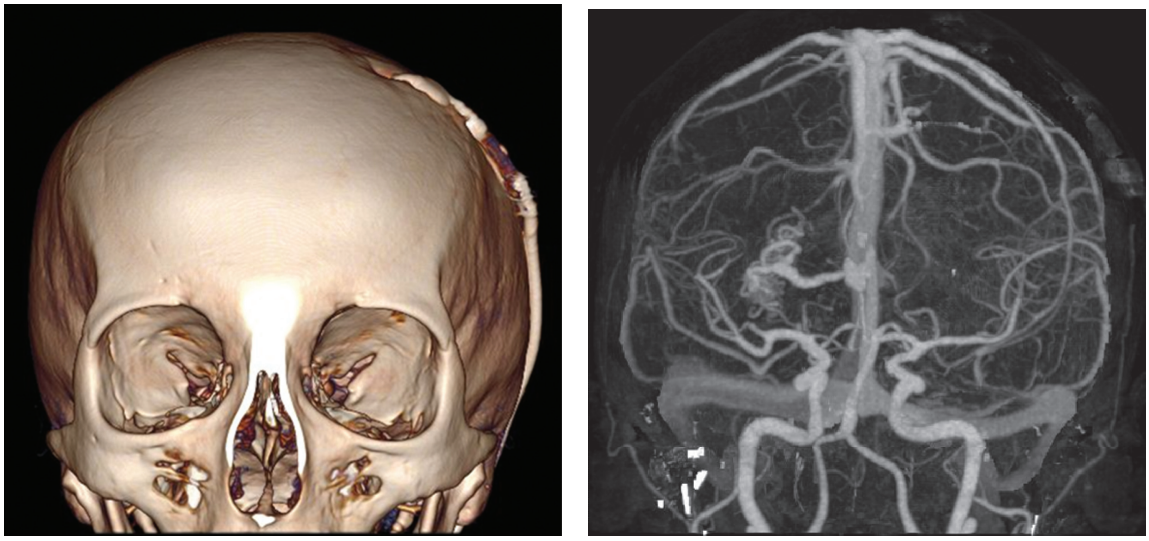

(a) (b)

FIGURE 1.18
Bone subtraction CT angiography (CTA) in a patient with arteriovenous malformation: (a) A nonenhanced (low-dose) CT can be used to create a three-dimensional bone model, which can be registered with a CTA to automatically suppress bone while maintaining soft tissues and vessels (b) (maximum intensity projection).

preprocessing is performed [73–78]. BSCTA can also be applied successfully in peripheral CTA [79].

An alternative to BSCTA is DECT, where simultaneous data acquisition at two energy levels is performed (see earlier) and calcium can be easily differentiated from iodine by the different absorptions at 140 kV and 80/100 kV [40].

References

1. Crawford CR, King KF. Computed tomography scanning with simultaneous patient translation. *Med Phys* 1990;17:967–982.
2. Kalender WA, Seissler W, Klotz E, Vock P. Spiral volumetric CT with single-breath-hold technique, continuous transport, and continuous scanner rotation. *Radiology* 1990;176:181–183.
3. Mori I. Computerized tomographic apparatus utilizing a radiation source. U.S. Patent 4630202, 1986.
4. Nishimura H, Miyazaki O. CT system for specially scanning subject on a moveable bed synchronized to x-ray tube revolution. U.S. Patent 4789929, 1988.
5. Kalender WA. Thin-section three-dimensional spiral CT: Is isotropic imaging possible? *Radiology* 1995;197: 578–580.
6. Hu H, He HD, Foley WD, Fox SH. Four multidetector-row helical CT: Image quality and volume coverage speed. *Radiology* 2000;215:55–62.
7. Klingenbeck-Regn K, Schaller S, Flohr T, Ohnesorge B, Kopp AF, Baum U. Subsecond multi-slice computed tomography: Basics and applications. *Eur J Radiol* 1999;31:110–124.
8. Kachelriess M, Ulzheimer S, Kalender WA. ECG-correlated image reconstruction from subsecond multi-slice spiral CT scans of the heart. *Med Phys* 2000;27: 1881–1902.
9. Ohnesorge B, Flohr T, Becker C et al. Cardiac imaging by means of electrocardiographically gated multisection spiral CT: Initial experience. *Radiology* 2000;217:564–571.
10. Nieman K, Oudkerk M, Rensing BJ et al. Coronary angiography with multi-slice computed tomography. *Lancet* 2001;357:599–603.
11. Lell MM, Anders K, Uder M et al. New techniques in CT angiography. *Radiographics* 2006;26 Suppl 1:S45–S62.
12. Flohr TG, McCollough CH, Bruder H et al. First performance evaluation of a dual-source CT (DSCT) system. *Eur Radiol* 2006;16:256–268.
13. Flohr TG, Stierstorfer K, Ulzheimer S, Bruder H, Primak AN, McCollough CH. Image reconstruction and image quality evaluation for a 64-slice CT scanner with *z*-flying focal spot. *Med Phys* 2005;32:2536–2547.
14. Flohr TG, Schaller S, Stierstorfer K, Bruder H, Ohnesorge BM, Schoepf UJ. Multi-detector row CT systems and image-reconstruction techniques. *Radiology* 2005;235: 756–773.
15. Schardt P, Deuringer J, Freudenberger J et al. New x-ray tube performance in computed tomography by introducing the rotating envelope tube technology. *Med Phys* 2004;31:2699–2706.
16. Hsieh J. Investigation of the slice sensitivity profile for step-and-shoot mode multi-slice computed tomography. *Med Phys* 2001;28:491–500.
17. Hsieh J. Analytical models for multi-slice helical CT performance parameters. *Med Phys* 2003;30:169–178.
18. Hu H. Multi-slice helical CT: Scan and reconstruction. *Med Phys* 1999;26:5–18.
19. Taguchi K, Aradate H. Algorithm for image reconstruction in multi-slice helical CT. *Med Phys* 1998;25:550–561.

20. Feldkamp LA, Davis LC, Kress JW. Practical cone-beam algorithm. *J Opt Soc Am A* 1984;1:612–619.
21. Flohr T, Stierstorfer K, Bruder H, Simon J, Polacin A, Schaller S. Image reconstruction and image quality evaluation for a 16-slice CT scanner. *Med Phys* 2003; 30:832–845.
22. Mark DB, Berman DS, Budoff MJ et al. ACCF/ACR/AHA/NASCI/SAIP/SCAI/SCCT 2010 expert consensus document on coronary computed tomographic angiography: A report of the American College of Cardiology Foundation Task Force on Expert Consensus Documents. *Circulation* 2010;121:2509–2543.
23. Dewey M, Zimmermann E, Deissenrieder F et al. Noninvasive coronary angiography by 320-row computed tomography with lower radiation exposure and maintained diagnostic accuracy: Comparison of results with cardiac catheterization in a head-to-head pilot investigation. *Circulation* 2009;120:867–875.
24. Diekmann S, Siebert E, Juran R et al. Dose exposure of patients undergoing comprehensive stroke imaging by multidetector-row CT: Comparison of 320-detector row and 64-detector row CT scanners. *AJNR Am J Neuroradiol* 2010;31:1003–1009.
25. George RT, Arbab-Zadeh A, Cerci RJ et al. Diagnostic performance of combined noninvasive coronary angiography and myocardial perfusion imaging using 320-MDCT: The CT angiography and perfusion methods of the CORE320 multicenter multinational diagnostic study. *AJR Am J Roentgenol* 2011;197:829–837.
26. Klingebiel R, Siebert E, Diekmann S et al. 4-D imaging in cerebrovascular disorders by using 320-slice CT: Feasibility and preliminary clinical experience. *Acad Radiol* 2009;16:123–129.
27. Achenbach S, Marwan M, Schepis T et al. High-pitch spiral acquisition: A new scan mode for coronary CT angiography. *J Cardiovasc Comput Tomogr* 2009;3:117–121.
28. Hausleiter J, Bischoff B, Hein F et al. Feasibility of dual-source cardiac CT angiography with high-pitch scan protocols. *J Cardiovasc Comput Tomogr* 2009;3:236–242.
29. Lell M, Marwan M, Schepis T et al. Prospectively ECG-triggered high-pitch spiral acquisition for coronary CT angiography using dual source CT: Technique and initial experience. *Eur Radiol* 2009;19:2576–2583.
30. Johnson TR, Krauss B, Sedlmair M et al. Material differentiation by dual energy CT: Initial experience. *Eur Radiol* 2007;17:1510–1517.
31. Primak AN, Fletcher JG, Vrtiska TJ et al. Noninvasive differentiation of uric acid versus non-uric acid kidney stones using dual-energy CT. *Acad Radiol* 2007;14: 1441–1447.
32. Scheffel H, Stolzmann P, Frauenfelder T et al. Dual-energy contrast-enhanced computed tomography for the detection of urinary stone disease. *Invest Radiol* 2007;42:823–829.
33. Ertel D, Lell MM, Harig F, Flohr T, Schmidt B, Kalender WA. Cardiac spiral dual-source CT with high pitch: A feasibility study. *Eur Radiol* 2009;19:2357–2362.
34. Lell MM, May M, Deak P et al. High-pitch spiral computed tomography: Effect on image quality and radiation dose in pediatric chest computed tomography. *Invest Radiol* 2011;46:116–123.
35. Alvarez RE, Macovski A. Energy-selective reconstructions in X-ray computerized tomography. *Phys Med Biol* 1976;21:733–744.
36. Avrin DE, Macovski A, Zatz LE. Clinical application of Compton and photo-electric reconstruction in computed tomography: Preliminary results. *Invest Radiol* 1978;13:217–222.
37. Kalender WA, Perman WH, Vetter JR, Klotz E. Evaluation of a prototype dual-energy computed tomographic apparatus. I. Phantom studies. *Med Phys* 1986;13:334–339.
38. Glazebrook KN, Guimaraes LS, Murthy NS et al. Identification of intraarticular and periarticular uric acid crystals with dual-energy CT: Initial evaluation. *Radiology* 2011;261:516–524.
39. Graser A, Becker CR, Staehler M et al. Single-phase dual-energy CT allows for characterization of renal masses as benign or malignant. *Invest Radiol* 2010;45:399–405.
40. Lell MM, Kramer M, Klotz E, Villablanca P, Ruehm SG. Carotid computed tomography angiography with automated bone suppression: A comparative study between dual energy and bone subtraction techniques. *Invest Radiol* 2009;44:322–328.
41. Lu GM, Wu SY, Yeh BM, Zhang LJ. Dual-energy computed tomography in pulmonary embolism. *Br J Radiol* 2010; 83:707–718.
42. Thibault JB, Sauer KD, Bouman CA, Hsieh J. A three-dimensional statistical approach to improved image quality for multislice helical CT. *Med Phys* 2007;34:4526–4544.
43. Donnelly LF, Emery KH, Brody AS et al. Minimizing radiation dose for pediatric body applications of single-detector helical CT: Strategies at a large Children's Hospital. *AJR Am J Roentgenol* 2001;176:303–306.
44. Wildberger JE, Mahnken AH, Schmitz-Rode T et al. Individually adapted examination protocols for reduction of radiation exposure in chest CT. *Invest Radiol* 2001;36:604–611.
45. May MS, Wust W, Brand M et al. Dose reduction in abdominal computed tomography: Intraindividual comparison of image quality of full-dose standard and half-dose iterative reconstructions with dual-source computed tomography. *Invest Radiol* 2011; 46:465–470.
46. Katsura M, Matsuda I, Akahane M et al. Model-based iterative reconstruction technique for radiation dose reduction in chest CT: Comparison with the adaptive statistical iterative reconstruction technique. *Eur Radiol* 2012;22:1613–1623.
47. Leipsic J, Nguyen G, Brown J, Sin D, Mayo JR. A prospective evaluation of dose reduction and image quality in chest CT using adaptive statistical iterative reconstruction. *AJR Am J Roentgenol* 195:1095–1099.
48. Pontana F, Duhamel A, Pagniez J et al. Chest computed tomography using iterative reconstruction vs filtered back projection (Part 2): Image quality of low-dose CT examinations in 80 patients. *Eur Radiol* 21:636–643.
49. Prakash P, Kalra MK, Digumarthy SR et al. Radiation dose reduction with chest computed tomography using adaptive statistical iterative reconstruction technique: Initial experience. *J Comput Assist Tomogr* 2010;34:40–45.

50. Greess H, Lutze J, Nomayr A et al. Dose reduction in subsecond multislice spiral CT examination of children by online tube current modulation. *Eur Radiol* 2004;14:995–999.
51. Greess H, Wolf H, Suess C, Kalender WA, Bautz W, Baum U. [Automatic exposure control to reduce the dose in subsecond multislice spiral CT: Phantom measurements and clinical results]. *Rofo* 2004;176:862–869.
52. Mulkens TH, Bellinck P, Baeyaert M et al. Use of an automatic exposure control mechanism for dose optimization in multi-detector row CT examinations: Clinical evaluation. *Radiology* 2005;237:213–223.
53. Ketelsen D, Buchgeister M, Fenchel M et al. Automated computed tomography dose-saving algorithm to protect radiosensitive tissues: Estimation of radiation exposure and image quality considerations. *Invest Radiol* 2012;47:148–152.
54. Winklehner A, Goetti R, Baumueller S et al. Automated attenuation-based tube potential selection for thoracoabdominal computed tomography angiography: Improved dose effectiveness. *Invest Radiol* 2011;46:767–773.
55. Eller A, May MS, Scharf M et al. Attenuation-based automatic kilovolt selection in abdominal computed tomography: Effects on radiation exposure and image quality. *Invest Radiol* 2012;47:559–565.
56. Neefjes LA, Dharampal AS, Rossi A et al. Image quality and radiation exposure using different low-dose scan protocols in dual-source CT coronary angiography: Randomized study. *Radiology* 261:779–786.
57. Achenbach S, Marwan M, Ropers D et al. Coronary computed tomography angiography with a consistent dose below 1 mSv using prospectively electrocardiogram-triggered high-pitch spiral acquisition. *Eur Heart J* 2010;31:340–346.
58. Christner JA, Zavaletta VA, Eusemann CD, Walz-Flannigan AI, McCollough CH. Dose reduction in helical CT: Dynamically adjustable *z*-axis X-ray beam collimation. *AJR Am J Roentgenol* 2010;194:W49–W55.
59. Deak PD, Langner O, Lell M, Kalender WA. Effects of adaptive section collimation on patient radiation dose in multisection spiral CT. *Radiology* 2009;252:140–147.
60. Stacul F, van der Molen AJ, Reimer P et al. Contrast induced nephropathy: Updated ESUR Contrast Media Safety Committee guidelines. *Eur Radiol* 2011;21: 2527–2541.
61. Bae KT. Intravenous contrast medium administration and scan timing at CT: Considerations and approaches. *Radiology* 2010;256:32–61.
62. Muhlenbruch G, Behrendt FF, Eddahabi MA et al. Which Iodine concentration in chest CT?—A prospective study in 300 patients. *Eur Radiol* 2008;18:2826–2832.
63. Fleischmann D, Rubin GD, Bankier AA, Hittmair K. Improved uniformity of aortic enhancement with customized contrast medium injection protocols at CT angiography. *Radiology* 2000;214:363–371.
64. Fleischmann D. Use of high concentration contrast media: principles and rationale-vascular district. *Eur J Radiol* 2003;45 Suppl 1:S88–S93.
65. Fleischmann D. Present and future trends in multiple detector-row CT applications: CT angiography. *Eur Radiol* 2002;12 Suppl 2:S11–S15.
66. Flohr TG, Stierstorfer K, Suss C, Schmidt B, Primak AN, McCollough CH. Novel ultrahigh resolution data acquisition and image reconstruction for multi-detector row CT. *Med Phys* 2007;34:1712–1723.
67. Calhoun PS, Kuszyk BS, Heath DG, Carley JC, Fishman EK. Three-dimensional volume rendering of spiral CT data: Theory and method. *Radiographics* 1999;19:745–764.
68. Udupa JK. Three-dimensional visualization and analysis methodologies: A current perspective. *Radiographics* 1999;19:783–806.
69. Hame Y, Pollari M. Semi-automatic liver tumor segmentation with hidden Markov measure field model and non-parametric distribution estimation. *Med Image Anal* 2012;16:140–149.
70. Schumann C, Bieberstein J, Braunewell S, Niethammer M, Peitgen HO. Visualization support for the planning of hepatic needle placement. *Int J Comput Assist Radiol Surg* 2012;7:191–197.
71. Linguraru MG, Pura JA, Chowdhury AS, Summers RM. Multi-organ segmentation from multi-phase abdominal CT via 4D graphs using enhancement, shape and location optimization. *Med Image Comput Comput Assist Interv* 2010;13:89–96.
72. Heimann T, van Ginneken B, Styner MA et al. Comparison and evaluation of methods for liver segmentation from CT datasets. *IEEE Trans Med Imaging* 2009;28:1251–1265.
73. Lell MM, Ruehm SG, Kramer M et al. Cranial computed tomography angiography with automated bone subtraction: A feasibility study. *Invest Radiol* 2009;44:38–43.
74. Loeckx D, Coudyzer W, Maes F et al. Nonrigid registration for subtraction CT angiography applied to the carotids and cranial arteries. *Acad Radiol* 2007;14:1562–1576.
75. Lell MM, Ditt H, Panknin C et al. Bone-subtraction CT angiography: Evaluation of two different fully automated image-registration procedures for interscan motion compensation. *AJNR Am J Neuroradiol* 2007;28:1362–1368.
76. Tomandl BF, Hammen T, Klotz E, Ditt H, Stemper B, Lell M. Bone-subtraction CT angiography for the evaluation of intracranial aneurysms. *AJNR Am J Neuroradiol* 2006;27:55–59.
77. Lell M, Anders K, Klotz E, Ditt H, Bautz W, Tomandl BF. Clinical evaluation of bone-subtraction CT angiography (BSCTA) in head and neck imaging. *Eur Radiol* 2006;16:889–897.
78. van Straten M, Venema HW, Streekstra GJ, Majoie CB, den Heeten GJ, Grimbergen CA. Removal of bone in CT angiography of the cervical arteries by piecewise matched mask bone elimination. *Med Phys* 2004;31:2924–2933.
79. Lee IJ, Chung JW, Hong H et al. Subtraction CT angiography of the lower extremities: Single volume subtraction versus multi-segmented volume subtraction. *Acad Radiol* 2011;18:902–909.

2

CT Perfusion: Principles, Implementations, and Clinical Applications

Aaron So, Errol E. Stewart, Christopher D. d'Esterre, Timothy Pok Chi Yeung, Glenn Bauman, Nikolaj K. G. Jensen, Eugene Wong, and Ting-Yim Lee

CONTENTS

2.1 Introduction

Shortly after the introduction of computed tomography (CT) in 1970s, a seminal paper by Leon Axel demonstrated the use of dynamic contrast-enhanced (DCE) CT to measure tissue blood flow (perfusion) [1]. This perfusion imaging capability has since transformed CT from an anatomic-oriented imaging modality into a functional one, allowing comprehensive assessment of structural and physiologic abnormalities in a single sitting. Initially, CT perfusion (CTP) was mainly confined to research rather than clinical studies due to the requirement of rapid image acquisition. With the advent of multirow detectors [2,3] and faster speed of gantry rotation [4] in clinical CT scanners, CTP has gained popularity over the past decade as a diagnostic tool for stroke [5–7], tumor [8–11], and more recently coronary artery disease (CAD) [12–15]. Having these diagnostic capabilities coupled with the operational advantages of low cost, accessibility, and high throughput of CT, it is expected that CTP will play a more and more important role on patient management.

All CTP methodologies require intravenous (IV) bolus administration of iodinated contrast medium and are dependent on the excellent linear relationship between x-ray attenuation and concentration of contrast material in tissue and blood. The first-pass bolus tracking perfusion analysis techniques are based on one of the three theories: indicator-dilution, Fick principle, and deconvolution. In this chapter, we aim to review the fundamental basis of each CTP method, followed by the technical considerations for implementations. Preclinical validations and clinical applications of deconvolution-based CTP methodology are also presented.

2.2 Basic Model and Terminology

For ease of discussion, let us first consider the schematic in Figure 2.1, which represents a unit mass of tissue. The inlet and outlet orifices represent an input artery (arteriole) and a draining vein (venule) of the tissue. "Blood flow" (F) through the tissue, or perfusion, is defined as the volume of blood that is moving through the vasculature of the tissue per unit time. It is expressed in units of $mL/min^{-1}/g^{-1}$. In CTP, perfusion is usually modeled as a plug of fluid (plug flow) through the vasculature, in which the flow velocity profile across the cross section

of the vessels is constant. Additionally, "blood volume" (V) is defined as the volume of blood within the vasculature in the tissue that is flowing (nonstatic). It is expressed in mL/g^{-1}. In reality, there are numerous small capillaries interconnecting with each other rather than a single capillary tube in the tissue (Figure 2.1c and d). Thus, upon arrival at the arterial inlet, contrast solutes can take different paths to reach the venous exit. As such, there exists a distribution of transit times, which can be described by a frequency or probability density function of transit time through a vascular bed, $h(t)$, as shown in Figure 2.2a. The integral of the probability density function, $H(t)$, describes the fraction of contrast solutes that has left the tissue at time t (Figure 2.2b). The total amount of contrast solutes that has left the tissue should increase with time and eventually reach the plateau at unity. This can be explained by the fact that all contrast solutes introduced into the tissue will eventually leave the tissue in due time, and the total amount of contrast leaving the tissue cannot exceed the amount that is introduced into the tissue. It follows that the residual function, $R(t)$, which describes the fraction of contrast solutes, remains in the tissue at time t, is equal to $1 - H(t)$ (Figure 2.2c), with the area under curve (AUC) of $R(t)$ equals the "mean transit time" (MTT)—the average time required for the contrast solutes to travel from the arterial inlet to the venous outlet of the tissue (Figure 2.2d) [16,17].

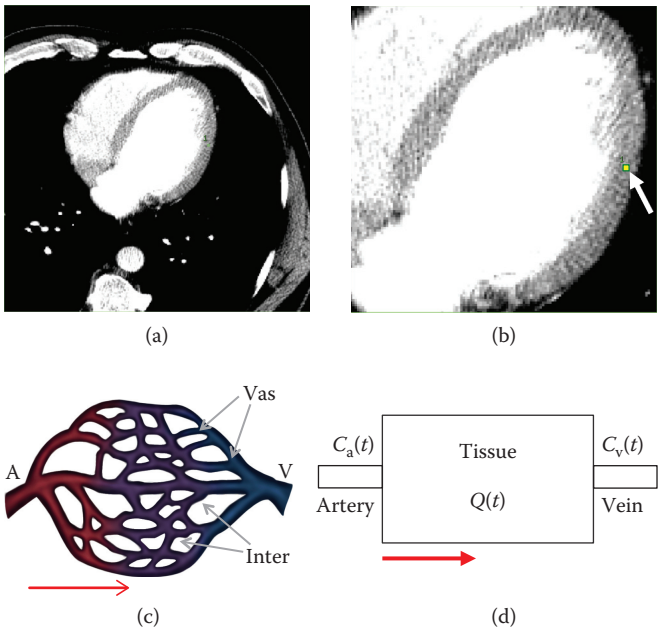

FIGURE 2.1
(a) Contrast-enhanced CT image of a patient's heart. (b) A voxel of interest in the myocardium. (c) Schematic of the vasculature of a tissue within the voxel shown in Figure 2.1b. The red arrow denotes the direction of blood flow through the capillaries from arteriole (A) to venule (V). (d) A simple model represents the vasculature in Figure 2.1c. The tissue region consists of the capillaries (intravascular space, vas) and the surrounding interstitium (interstitial space, inter). The relationship between the concentration of contrast medium in the input artery ($C_a(t)$) and draining vein ($C_v(t)$) and the mass of contrast in tissue ($Q(t)$) is governed by Fick principle. The exchange of contrast between the intravascular and interstitial spaces is described by the tracer kinetic models shown in Figures 2.5 and 2.6.

During a single capillary transit, contrast solutes can diffuse across the permeable endothelium (consists of a single cell layer) to the surrounding interstitial (extravascular) space. One exception is the healthy brain tissue, where the blood–brain barrier (BBB), consisting of tight junctions between endothelial cells, surrounding basement membrane, and astrocytic foot processes, restricts most of the diffusions taking place [18]. The transport of contrast solutes from the intravascular to interstitial space is driven entirely by passive diffusion (concentration gradient between the two spaces). The "extraction fraction," E, describes the fraction of contrast solutes diffused from the intravascular to interstitial space during

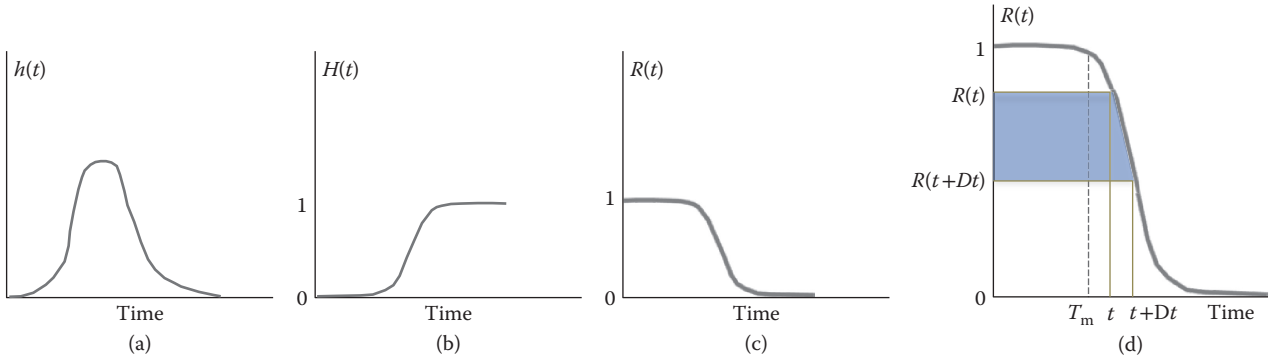

FIGURE 2.2
(a) The frequency function, $h(t)$, describes the distribution of transit time through a vasculature bed in tissue after a bolus injection of contrast. (b) Integral of the frequency function in Figure 2.2a, $H(t)$, describes the fraction of contrast that has left the system as a function of time. (c) The total amount of contrast remains in the tissue as a function of time is given by $1 - H(t)$, or $R(t)$. (d) Beyond the minimum transit time, T_m, the fraction of contrast that leaves the tissue between t and $t + \Delta t$ is equal to the difference of $R(t + \Delta t)$ and $R(t)$ (blue section). This fraction of contrast medium has a transit time of Δt. It follows that the total area under $R(t)$ is equivalent to the mean transit time (MTT).

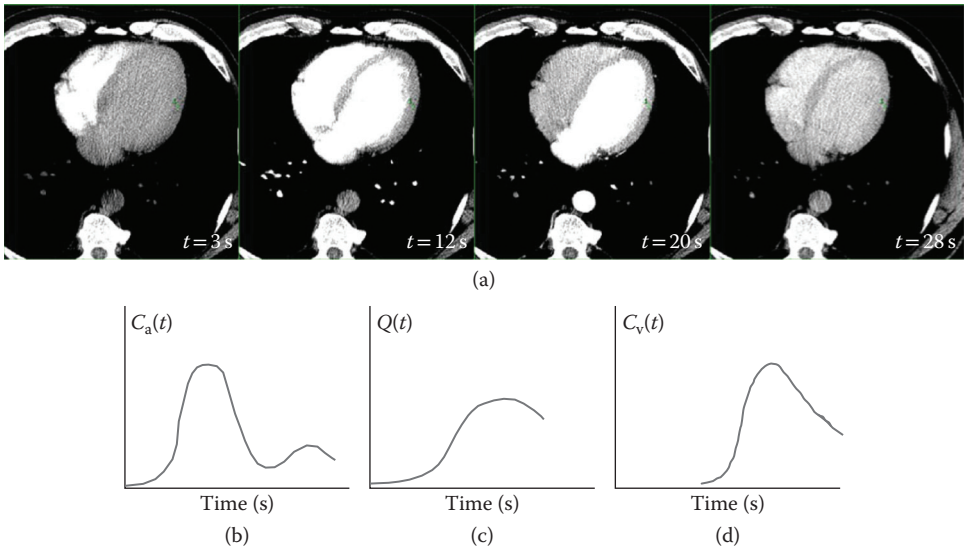

FIGURE 2.3
(a) DCE CT images of the same patient's heart in Figure 2.1 at different time points. Iodinated contrast medium circulated in the heart chambers and aorta during the time of imaging. The time postbolus injection of contrast of each image is shown in the bottom right corner. Schematics of typical arterial, tissue, and venous TDC measured from DCE CT images are shown in Figure 2.3b, c, and d, respectively.

a single passage from the arterial to venous ends of the capillaries [19]. E can be represented by the following equation:

$$E = 1 - e^{-\frac{PS}{F}} \tag{2.1}$$

where PS is "permeability surface area product"—the product of permeability and the total surface area of capillary endothelium in a unit mass of tissue and hence is the total diffusional flux across all capillaries [19]. It is measured in units of $mL/min^{-1}/g^{-1}$.

After the introduction of a bolus of iodinated contrast material, repeated rapid CT scanning is acquired at the same location to allow determination of time-density curves (TDCs). Figure 2.3 illustrates the typical shape of arterial ($C_a(t)$), tissue ($Q(t)$), and venous ($C_v(t)$) TDCs acquired from DCE CT scanning. Several methods that are commonly used for analyzing these TDCs to derive perfusion values are reviewed in Sections 2.2.1 through 2.2.5.

2.2.1 Indicator-Dilution Method

Indictor-dilution method was originally proposed over a century ago to measure blood velocity (circulation time) and cardiac output [20]. It was then shown that this technique could also be used to measure tissue blood flow (perfusion) [16,21]. This technique is based on the fact that after administration into the circulation, the degree at which tracer molecules (e.g., CT contrast medium, radiolabeled particles, or dye) are mixed with blood (i.e., dilution) is dependent on blood flow. The indicator-dilution method has since been modified to measure blood flow in tissue using dynamic CT scanning [1,22]. The basis of the method is briefly reviewed here. If a voxel of interest in a CT image is devoid of major blood vessels, the concentration of contrast medium in the tissue in this voxel at time t, $C_t(t)$, should be lower than that in the vascular space, $C_a(t)$, by the fraction f:

$$C_t(t) = f \cdot C_a(t) \tag{2.2}$$

where f is defined as

$$f = \frac{V_b}{V_b + V_e + V_{cell}} \tag{2.3}$$

with V_b, V_e, and V_{cell} being the distribution volumes of contrast medium in the vascular space, interstitial space, and cell(s), respectively. Equations 2.2 and 2.3 suggest that f is essentially the blood volume in tissue, which can be estimated by dividing the AUC of the tissue TDC to the AUC of the arterial TDC.

$$V = \frac{AUC_{tissue}}{AUC_{artery}} \tag{2.4a}$$

$$AUC_{tissue} = \int_0^T C_t(t)\,dt \tag{2.4b}$$

$$AUC_{artery} = \int_0^T C_a(t)\,dt \tag{2.4c}$$

Once the blood volume in tissue is determined, perfusion can be calculated as the ratio of V to the MTT according to the central volume principle [16].

$$F = \frac{V}{\text{MTT}} \tag{2.5}$$

MTT cannot be measured directly but can be estimated from either deconvolution [23] or the center of gravity [22] of the arterial and tissue TDCs:

$$\text{MTT} = C \cdot \left[<\text{tissue}> - <\text{artery}> \right] \tag{2.6a}$$

$$= C \cdot \left[\frac{\int_0^T t \cdot C_t(t)\,dt}{\int_0^T C_t(t)\,dt} - \frac{\int_0^T t \cdot C_a(t)\,dt}{\int_0^T C_a(t)\,dt} \right] \tag{2.6b}$$

where <tissue> and <artery> represent the centers of gravity of these two TDCs and the center of gravity of each curve is calculated as the first moment of the curve (which can be viewed as a quantitative measure of the shape of the curve) as in Equation 2.6b; C is a combined correction factor to account for the difference between large vessel (vein or artery) and small vessel (tissue) hematocrit, the difference between contrast arrival times at the measured artery (true input artery to the region of interest [ROI]) and tissue, and the variations in transit times through the ROI to the difference in the first moments of tissue and artery TDCs (<tissue> – <artery>) [22]. Although the indicator-dilution method is mathematically more simple than the deconvolution method, this technique has a few major limitations. First, the method relies heavily on the accuracy of blood volume estimate. For healthy brain tissue, contrast medium remains in the intravascular space throughout the capillary transit. However, in abnormal brain tissue where the BBB is no longer intact [24,25], and in other tissues such as the heart and liver [19], extravascular leakage of contrast may occur, which will lead to overestimation of blood volume and hence blood flow. Second, the correction factor, C, assumes a certain geometry/topology of the vasculature (or transit time distribution) that makes the method model dependent after all.

2.2.2 Maximal Slope Method

The relationship between tissue blood flow, the amount (mass) of contrast medium that remains in the tissue, and the concentration of contrast medium at the input artery and draining vein can be described using the Fick principle. If we denote $C_a(t)$ and $C_v(t)$ as the contrast concentration in the arterial inlet and venous outlet of the tissue at time t, respectively, and F is the tissue blood flow (perfusion) during the time of study, the influx and efflux rates of contrast are given by $F \cdot C_a(t)$ and $F \cdot C_v(t)$, respectively. Under the assumption of conservation of mass, the following relationship holds:

$$\frac{dQ(t)}{dt} = F \cdot C_a(t) - F \cdot C_v(t) \tag{2.7}$$

where $Q(t)$ is the mass of contrast in the tissue at time t. Equation 2.7 states that the rate of change of the mass of contrast in the tissue is equal to the difference in the influx and efflux rates of contrast. Integrating equation 2.7 yields

$$Q(t) = F \cdot \int^T [C_a(t) - C_v(t)] \cdot dt \tag{2.8}$$

Equation 2.8 states that the accumulated mass of contrast in the tissue over the duration of acquisition, from 0 to T, is equal to the product of flow and the time integral of the difference in the arterial and venous concentration of contrast medium. One simplification that would make solving Equation 2.8 easier is to assume no venous outflow of contrast in tissue during the time of study ($C_v(t) = 0$). If the no venous outflow assumption is valid, Equation 2.8 is simplified to [26]

$$Q(t) = F \cdot \int_0^T C_a(t) \cdot dt \tag{2.9}$$

By taking the differentiation on both sides of Equation 2.9 yields

$$\frac{dQ(t)}{dt} = F \cdot C_a(t) \tag{2.10}$$

Equation 2.10 suggests the rate of contrast accumulation in tissue will be maximal when the arterial concentration of contrast reaches maximum.

$$\left.\frac{dQ(t)}{dt}\right|_{\max} = F \cdot C_a(t)\big|_{\max}$$

$$F = \left.\frac{\frac{dQ(t)}{dt}}{C_a(t)}\right|_{\max} \tag{2.11}$$

It follows that F can be estimated by dividing the maximal slope of $Q(t)$ by the maximal arterial concentration (peak value of arterial TDC). This is known as the maximal slope method.

The advantage of the maximal slope method is its computational simplicity. Additionally, only the upslope of the TDCs used for perfusion analysis implies acquisition of the entire bolus curves is not necessary, which can reduce radiation exposure to the patients. However, the assumption of no venous outflow may not be valid in all disease states. To make the no venous outflow assumption more valid in practice, the bolus injection rate has to be very fast,

usually >10 mL/s^{-1} [27,28], which is not always practical in clinical settings. As such, the assumption could be violated in real situations, which may lead to significant underestimation of the true perfusion value. An alternative solution to fast injection rate is to inject a less amount of contrast material but at a slower rate. However, this will lead to a poorer signal-to-noise ratio (SNR) of the TDC, which in turn will affect the accuracy of perfusion estimates.

2.2.3 Deconvolution Method

The deconvolution method takes a different approach and handles the contrast enhancement tissue/organ from perfusion as a time-invariant linear system problem. For reference, we will first briefly review the characteristics of such a system.

Figure 2.4 illustrates an output signal in response to an impulse signal presented to such a system. Both the input and the output signals are plotted as signal intensity versus time. An impulse signal is instantaneous and transient and can be represented by a Dirac delta function, which is defined as infinite at $t = 0$ but with an area of unity (for simplicity, we will say that impulse has a magnitude of unity) and zero elsewhere (i.e., $t > 0$) (Figure 2.4a). The output signal consists of a single step of finite width followed by an exponential tail (Figure 2.4b). The step

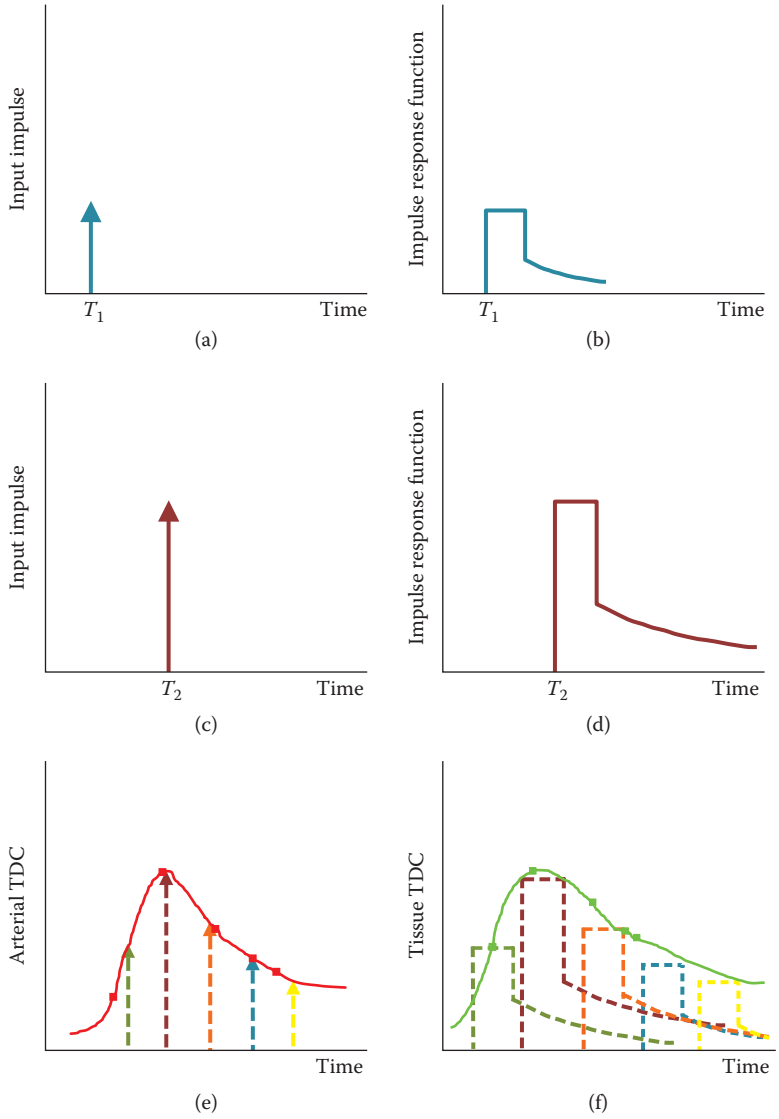

FIGURE 2.4
(a) An impulse signal to a time-invariant linear system and (b) the corresponding IRF. (c) A second impulse signal with twice the magnitude as the first impulse introduced to the system at a later time, and (d) the corresponding IRF to the second impulse. (e) An arterial TDC measured from DCE CT scanning can be interpreted as a superimposition of sequential impulses with different magnitudes at different times. (f) The corresponding tissue TDC can be viewed as a superimposition of the IRFs scaled by the magnitude and shifted in time to match those of the impulse signals.

has the height as the area underneath the impulse signal, which is unity, providing there is no signal lost in the linear system. Here, the width of the step corresponds to the minimum time required by the contrast to traverse the vasculature, whereas the tail describes the gradual decline of the signal over time from the washout of contrast from the tissue region (for intravascular contrast it would be washout from the vasculature). Now, consider a second impulse with twice the magnitude as the first impulse is introduced at a later time, the corresponding output signal would have a step that is twice as high and delayed with respect to the first output signal by the time interval between the two impulses (Figure 2.4c and d).

The output signal in response to a unit area impulse is also called the impulse response function (IRF), which provides useful information about the characteristic of the time-invariant linear system and allows one to infer how the system will respond to different stimuli. In CTP, the arterial TDC, $C_a(t)$, acquired with an arterial ROI in an artery from dynamic images obtained by continuous rapid CT scanning after contrast injection, can be viewed as a superimposition of sequential impulse signals with different magnitudes at different times (Figure 2.4e). Similarly, the corresponding tissue TDC, $Q(t)$, is a superimposition of the IRFs scaled by the magnitude of corresponding impulse signal and shift in time to match that of the impulse signal, both of these information are provided by the arterial TDC (Figure 2.4f). The superimposition of the same IRF using information from arterial TDC is equivalent to the mathematical operation of convolution between the IRF and $C_a(t)$. Thus, the concentration of contrast medium in tissue at a given time t is controlled by three factors: local blood flow (F), concentration of contrast material in the input artery ($C_a(t)$), and the physiological properties of local vasculature (i.e., blood volume and permeability) as encapsulated in the IRF. The mathematical expression of this statement is [16]

$$\begin{aligned} Q(t) &= F \cdot C_a(t) \otimes R(t) \\ &= C_a(t) \otimes F \cdot R(t) \\ &= \int_0^t C_a(\tau) \cdot [F \cdot R(t-\tau)] d\tau \end{aligned} \tag{2.12}$$

where $\otimes$ is the convolution integral and $R(t)$ is the IRF. Deconvolution is the opposite mathematical operation to convolution that can be used to "remove" the effect of arterial concentration of contrast on the tissue TDC to arrive at the flow-scaled IRF, $F \cdot R(t)$, the height of which is equal to perfusion as $R(t)$ has a height of unity by definition.

Deconvolution can be executed using a number of algorithms; one example is linear least square regression with single value decomposition [29,30]. Deconvolution can be performed without model assumption for the IRF; however, the deconvolution process is highly sensitive to noise in the arterial and tissue TDCs [31,32]. In presence of noise, deconvolution could result in a flow scaled IRF whose form has no physiologic meaning but could still reproduce the measured tissue TDC after convolution with the measured arterial TDC. In practice, it is preferred to perform model-based deconvolution where the IRF is modeled with a few tissue parameters such as blood flow and volume and permeability surface product, and the deconvolution process is equivalent to estimation of this set of limited number of parameters. With this approach, the initial guess of $F \cdot R(t)$ constructed from the initial estimates of the model parameters is convolved by the measured arterial TDC to obtain a synthesized tissue TDC. The difference between the measured and synthesized tissue TDCs will be taken into consideration in the generation of the next set of model parameter estimates. This process is iteratively repeated until the difference between the measured and synthesized tissue TDCs is minimized.

In Section 2.2.4, the tracer kinetic models that are most frequently employed for the modeling of the IRF are briefly reviewed. The complexity of each model depends on the degree of assumption made to facilitate the solving of the governing mathematical equations of the model. It should be noted that regardless of the choice of model, there is always a compromise between mathematical complexity of the model and the practical limits set by the data (i.e., limited temporal and spatial resolution and SNR).

2.2.4 Tracer Kinetic Models

2.2.4.1 Modified Kety Model

As x-ray contrast agents are hydrophilic and metabolically inert, they are normally excluded from the intracellular space and not metabolized within the intravascular and interstitial space. As such, a two-compartment model can be used to describe the intravascular-interstitial exchange of contrast solutes through the permeable capillary endothelium [33–36]. This model assumes instantaneous mixing of contrast solutes upon arrival in the intravascular and interstitial spaces. In other words, the contrast concentration within these compartments changes only temporally not spatially. The rate of change of the amount of contrast material in the interstitial compartment can be described by the following equation:

$$V_e \frac{dC_e(t)}{dt} = k_1 \cdot C_b(t) - k_2 \cdot C_e(t) \tag{2.13a}$$

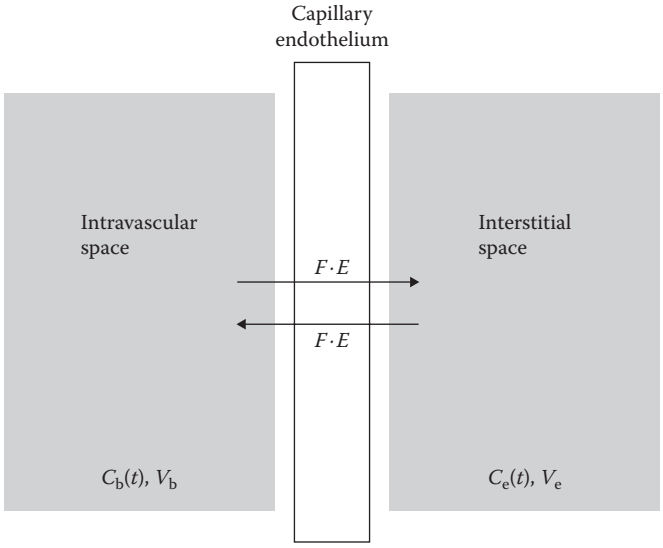

FIGURE 2.5
Diagram of a modified Kety (two-compartment) model used to describe the tracer kinetics in a tissue. The model assumes instantaneous mixing of contrast solutes upon arrival in blood and interstitium. Therefore, the concentration of contrast in the blood, C_b, and interstitium, C_e, are dependent on time t only. The governing rate constants of the forward and backward diffusion of contrast medium between these spaces are $F \cdot E$.

where V_e is the distribution volume of contrast solutes in the interstitial space, $C_e(t)$ and $C_b(t)$ are the concentration of contrast solutes in the interstitial and intravascular spaces, respectively. As contrast is assumed to be mixed instantaneously upon arrival, $C_b(t)$ is essentially equal to $C_a(t)$ as defined in Section 2.2.2. The variable k_1 is the forward transfer constant of contrast solutes from the intravascular to interstitial space and has a unit of min^{-1}, and similarly, k_2 is the backward transfer constant in min^{-1} from the interstitial to intravascular space. It has been shown that both k_1 and k_2 are equal to the product of flow and extraction fraction of the contrast solutes, or $F \cdot E$ [37]. A schematic of this model is provided in Figure 2.5. It should be emphasized that the vascular space represents all capillaries while the interstitial space represents the total interstitium outside all capillaries within a tissue. Equation 2.13a can be rewritten as follows:

$$\frac{dC_e(t)}{dt} = \frac{F \cdot E}{V_e}[C_a(t) - C_e(t)] \tag{2.13b}$$

The solution to Equation 2.13b is given by

$$C_e(t) = \frac{F \cdot E}{V_e} \cdot \int_0^t C_a(u) \cdot e^{-\frac{F \cdot E}{V_e}(t-u)} du \tag{2.14}$$

Because the mass of contrast in tissue measured by CT, $Q(t)$, is contributed by the contrasts in both the interstitial and the intravascular spaces

$$\begin{aligned} Q(t) &= C_e(t) \cdot V_e + C_a(t) \cdot V_b \\ &= F \cdot E \cdot \int_0^t C_a(u) \cdot e^{-\frac{F \cdot E}{V_e}(t-u)} du + C_a(t) \cdot V_b \end{aligned} \tag{2.15}$$

where V_b is the distribution volume of contrast in the intravascular space. According to the definition of convolution, Equation 2.15 can be rewritten as follows:

$$Q(t) = C_a(t) \otimes [F \cdot E \cdot e^{-\frac{F \cdot E}{V_e} \cdot t} + V_b \cdot \delta(t)] \tag{2.16}$$

where $\delta(t)$ is the Dirac delta function defined in Section 2.2.3. The convolution of $C_a(t)$ with $\delta(t)$ yields $C_a(t)$, as the integration of $\delta(t)$ is equal to unity. By comparing Equations 2.12 and 2.16, the flow-scaled IRF ($F \cdot R(t)$) of the two-compartment model has the following form:

$$F \cdot R(t) = V_b \tag{2.17a}$$

when $t = 0$

$$= F \cdot E \cdot e^{-\frac{F \cdot E}{V_e} \cdot t} \tag{2.17b}$$

when $t > 0$

Given the dynamic CT measurements of $C_a(t)$ and $Q(t)$, the parameters $F \cdot E$, V_b, and V_e can be estimated using nonlinear regression methods [38]. The advantage of compartmental modeling is its mathematical simplicity. The major drawback of this approach is that F and E cannot be estimated separately as they are determined together as a transport constant (k_1 and k_2). By assuming both the intravascular and interstitial spaces are well-stirred compartments, all the information relating to the convective transport of contrast solutes along the capillaries is lost. To estimate F, a constant value of E has to be assumed. This is a limitation as E is likely to be different among different tissue types (e.g., normal vs. ischemic vs. infarcted).

2.2.4.2 Patlak Model

The Patlak model is based on the modified Kety model discussed in Section 2.2.4.1, but with an additional assumption that the efflux of contrast solutes from the interstitial space back to the intravascular space is negligible [35,36]. This assumption implies the contrast distribution volume in the interstitial space (V_e) is very much larger relative to the backward transfer constant ($k_2 = F \cdot E$). Under this assumption, the ratio of $F \cdot E$ to V_e is close to zero, and the exponential term in Equation 2.16, $e^{-F \cdot E/V_e}$, is roughly equal to unity. The flow-scaled IRF, $F \cdot R(t)$, becomes

$$F \cdot R(t) = F \cdot E \cdot H(t) + V_b \cdot \delta(t) \tag{2.18}$$

where $H(t)$ is the Heaviside unit step function and is equal to zero at $t \leq 0$ and unity at $t > 0$. The unit step function, which by definition is zero at $t = 0$, is added in this equation to ensure the diffusion process, as governed by the forward transfer rate constant ($k_1 = F \cdot E$), does not start before the arrival of contrast solutes. Equation 2.15 then becomes

$$Q(t) = F \cdot E \int_0^t C_a(u)\,du + C_a(t) \cdot V_b \tag{2.19}$$

By dividing both sides by $C_a(t)$, Equation 2.19 can be rewritten as follows:

$$\frac{Q(t)}{C_a(t)} = F \cdot E \cdot \frac{\int_0^t C_a(u)\,du}{C_a(t)} + V_b \tag{2.20}$$

Equation 2.20 is a linear equation in the form of $y = mx + b$, where m and b are the slope and intercept, respectively. Thus, if $\frac{Q(t)}{C_a(t)}$ is plotted against $\frac{\int_0^t C_a(u)\,du}{C_a(t)}$, a straight line is produced with its slope equal to $F \cdot E$ and intercept equal to V_b. This method is known as the Patlak graphical plot. This approach can be interpreted as a mathematical transformation to "stretch" the measured tissue TDC into a straight-line plot. Unfortunately, the limitation of the modified Kety model also applies to the Patlak model, which is the fact that F and E cannot be determined separately. Another problem with the Patlak graphical method is that the no backward diffusion assumption may not be applicable in all situations.

2.2.4.3 Johnson and Wilson Model

Compared to the two-compartment (Kety) model, the Johnson and Wilson (J&W) model is a more realistic model to describe the kinetic behavior of contrast solutes in a single capillary transit. The J&W model is a distributed parameter model, which assumes a spatially nonuniform concentration gradient from the arterial to venous ends in the intravascular space to account for the potential loss of contrast solutes in blood via diffusion through the capillary endothelium [39]. Radial gradient of contrast concentration within the capillaries is neglected because convective (blood flow) transport of contrast in the axial direction is much larger than radial diffusion. In contrast to the intravascular space, the surrounding interstitial space is regarded as a compartment. This assumption is valid because capillaries in tissue are randomly oriented (Figure 2.1c); contrast solutes essentially diffuse into the interstitial space from all directions, which mimics a well-mixed compartment. From conservation of the mass of tracer (contrast) in both the intravascular and interstitial spaces, the J&W model leads to the following two equations describing the tracer transports during a single capillary transit:

$$\pi r^2 \frac{\partial C_b(x,t)}{\partial t} + \pi r^2 v \frac{\partial C_b(x,t)}{\partial x} = 2\pi r P\left(C_e(t) - C_b(x,t)\right) \tag{2.21a}$$

$$V_e \frac{\partial C_e(t)}{\partial t} = \int_0^l 2\pi r P\left(C_b(x,t) - C_e(x,t)\right) dx \tag{2.21b}$$

where r is the radius of the capillary; $C_b(x,t)$ is the concentration of contrast material within the capillary at time t and distance x relative to the arterial inlet; $C_e(t)$ is the concentration within the interstitial space at time t; v is the flow velocity of tracer; P is the permeability coefficient of the endothelial wall to the contrast; V_e is the distribution volume of contrast in the interstitial space; and l is the axial length of the capillary. A schematic of the J&W model is provided in Figure 2.6. Equation 2.21a describes the convective transport in the axial direction while equation 2.21b describes the diffusive transport of the contrast solutes between capillaries (intravascular) and interstitial space. As the total diffusional flux of contrast solutes is best described using

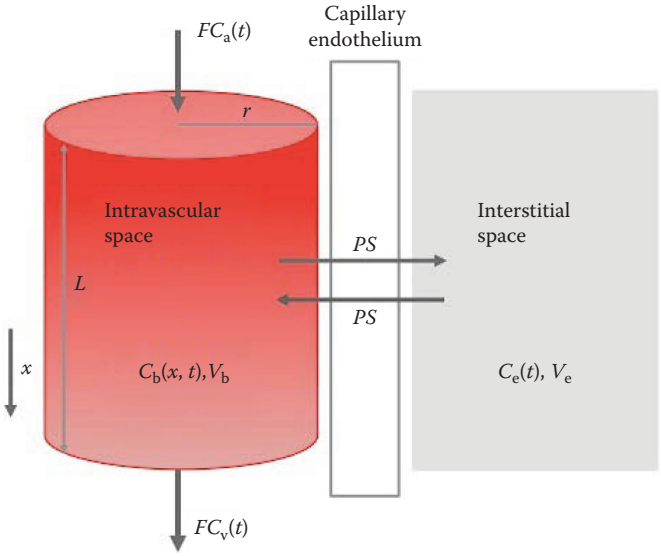

FIGURE 2.6
Diagram of a distributed parameter model (Johnson and Wilson model) used to describe the tracer kinetics in a tissue. According to the model, there is a concentration gradient of contrast medium in the capillaries along the flow direction as a result of potential diffusion across the endothelium into the interstitial space. Thus, $C_b(t)$ is a function of both the position in the capillaries (x) and time (t). The concentration gradient in the radical direction is assumed to be negligible. Diffusion of contrast across the capillary endothelium is governed by *PS*. The interstitial space is still considered as a compartment where contrast medium is instantaneously mixed with interstitium upon arrival.

the product of permeability coefficient (P) and the total surface area (S) of capillary endothelium, the preceding equations can be rewritten as follows:

$$\frac{\partial C_b(x,t)}{\partial t} + \frac{FL}{V_b}\frac{\partial C_b(x,t)}{\partial x} = \frac{PS}{V_b}[C_e(t) - C_b(x,t)] \quad (2.22a)$$

$$V_e \frac{dC_e(t)}{dt} = \frac{PS}{L}\int_0^L [C_b(x,t) - C_e(t)]dx \quad (2.22b)$$

Equations 2.22a and 2.22b are subject to the following initial and boundary conditions:

$$C_b(x, t=0) = C_e(t=0) = 0$$

$$C_b(x=0,\ t>0) = C_a(t) \quad (2.23)$$

The above initial and boundary conditions are justified by the fact that contrast concentration at $t = 0$ should be zero. Additionally, the concentration of contrast at the arterial end of the capillary is equal to the arterial concentration. Given the dynamic CT measurements of $C_a(t)$ and $Q(t)$, Laplace transform can be used to determine the solution of these equations, which satisfied the preceding boundary and initial conditions. As such, solutions to these differential equations only exist in the frequency domain, which significantly hamper the use of this tracer model [37]. It has been shown that a solution in the time domain can be derived by employing the adiabatic approximation, which assumes a much slower rate of change of contrast concentration in the interstitial space ($C_e(t)$) relative to that in the intravascular space ($C_b(x, t)$) [37]. With this assumption, $C_e(t)$ can be approximated by a sequence of discrete steps where $C_e(t)$ is constant within the duration of each step, which is much shorter than the capillary transit time. Within each discrete of $C_e(t)$, $C_b(x, t)$ can be expressed in terms of the constant $C_e(t)$ by solving Equation 2.22a [37]. The other details of the adiabatic approximation are outside the scope of this book chapter and are omitted here. The $F{\cdot}R(t)$ derived from the adiabatic solution has the following form:

$$F \cdot R(t) = \begin{cases} F & 0 < t < \text{MTT} \\ F \cdot E \cdot e^{-\frac{FE}{V_e}(t - T_c)} & t \geq \text{MTT} \end{cases} \quad (2.24)$$

According to the J&W model, there exists a finite transit time for contrast solutes to travel from the arterial to venous ends of the capillaries. As such, all contrast solutes should remain in the tissue within the MTT and is reflected by the plateau of the flow-scaled residual function. At $t = \text{MTT}$, $F \cdot R(t)$ immediately drops to a value of $F \cdot E$, as a portion $(1 - E)$ of contrast solutes begins to leave the tissue through the venous end and the fraction (E) diffused into the interstitial space is what remains in the tissue. The extracted contrast in the tissue follows a mono-exponential decay for $t >$ MTT, corresponding to the slower efflux from interstitial to vascular spaces and subsequent washout by blood flow [37].

2.2.5 Practical Issues of Tracer Kinetic Modeling

In a CTP study, the measured TDC may be affected by several factors. The potential effect of each factor on modeling of the IRF is reviewed in this section.

2.2.5.1 Recirculation of Contrast Medium

Recirculation refers to the reentry of contrast material to the organ/tissue of interest after previously leaving it and passing through the systematic circulation. Recirculation can occur as soon as 20–25 seconds after a bolus injection of contrast at 4 mL/s^{-1} (assuming 50 mL of contrast is administered and a normal resting heart rate and cardiac output of the patient). Thus, the effect of recirculation should be addressed in most CTP studies. Let us denote $C_a(t)_{fp}$ and $C_a(t)_r$ as the first-pass and recirculation components of an arterial TDC, respectively. Similarly, $Q(t)_{fp}$ and $Q(t)_r$ are the first-pass and recirculation components of a tissue TDC, respectively. With these definitions, $C_a(t)$ and $Q(t)$ are the summation of the two respective components.

$$C_a(t) = C_a^{fp}(t) + C_a^r(t) \quad (2.25a)$$

$$Q(t) = Q^{fp}(t) + Q^r(t) \quad (2.25b)$$

According to the convolution equation (Equation 2.12):

$$Q^{fp}(t) = C_a^{fp}(t) \otimes [F \cdot R(t)] \quad (2.26a)$$

$$Q^r(t) = C_a^r(t) \otimes [F \cdot R(t)] \quad (2.26b)$$

Substituting Equations 2.26a and 2.26b in Equation 2.25b, and according to the distributive property of convolution, we have

$$\begin{aligned} Q(t) &= Q^{fp}(t) + Q^r(t) \\ &= C_a^{fp}(t) \otimes \left[F \cdot R(t)\right] + C_a^r(t) \otimes [F \cdot R(t)] \\ &= \left[C_a^{fp}(t) + C_a^r(t)\right] \otimes [F \cdot R(t)] \end{aligned} \quad (2.27)$$

The preceding equation demonstrates that the $F{\cdot}R(t)$ can still be estimated from the measured arterial and tissue TDCs, with both containing the first-pass and

recirculation phases, using the deconvolution approach. Therefore, there is no need to correct for recirculation in the measured TDCs. Although the preceding derivation can be easily generalized to include more than one recirculation component, the effect of second or third recirculation component is expected to be negligible compared to the first recirculation component.

2.2.5.2 Dispersion in True Arterial TDC Relative to Measured Arterial TDC

Dispersion refers to the "spreading" of the arterial TDC at the true input site to a tissue region relative to the measurement site. An arterial TDC is normally acquired at a distance upstream to the tissue region to avoid significant partial volume effect owing to the small size of the local input artery (will be discussed in Section 2.3.5.1). In the presence of dispersion, the true and measured arterial TDCs satisfy the following relationship:

$$C_a(t) = C_a^m(t) \cdot h(t) \tag{2.28}$$

where $h(t)$, as introduced in Section 2.1, is the probability function or transit time spectrum that describes the various times required by individual contrast solute to travel from the measurement site to the actual arterial input site following a bolus injection. Substituting Equation 2.28 in Equation 2.12, and based on the associative property of convolution, yields

$$\begin{aligned} Q(t) &= [C_a^m(t) \cdot h(t)] \otimes F \cdot R(t) \\ &= C_a^m(t) \otimes [h(t) \otimes F \cdot R(t)] \end{aligned} \tag{2.29}$$

Equation 2.29 states that deconvolution of the measured arterial and tissue TDCs returns a flow-scaled residual function convolved with the arterial dispersion transit time spectrum. Previous phantom experiments suggested that the arterial TDC has negligible dispersion effect input curve if the measurement site is within 90 cm of the input site [37]. Thus, $h(t)$ can be approximated by a Dirac delta function, and Equation 2.29 is essentially identical to Equation 2.12. Hence, no dispersion correction is required for the arterial TDC as long as the measurement site is reasonably close to the true input site.

2.2.5.3 Delay of Tissue TDC Relative to Measured Arterial TDC

Because an arterial TDC is measured at a distance from the actual input site to a tissue region, there will be a slight time delay in the arrival of contrast in tissue relative to the measured arterial TDC. Such delay can be accounted for by making modifications to the equation for the IRF of each kinetics model. Let us denote $C_a^m(t)$ as the measured arterial TDC and T_o is the delay time relative to the measurement site.

$$C_a(t) = C_a^m(t - T_o) \tag{2.30}$$

Note that $(t - T_o)$ results in a positive time shift of the measured arterial TDC (as the true arterial TDC should lag behind the measured arterial TDC). Substituting Equation 2.30 in Equation 2.12 yields

$$\begin{aligned} Q(t) &= C_a(t) \cdot F \cdot R(t) = C_a^m(t - T_o) \cdot F \cdot R(t) \\ &= F \cdot \int_0^t C_a(t - T_o) \cdot R(t - \tau)\, d\tau \\ &= F \cdot \int_0^t C_a(t) \cdot R(t - T_o - \tau)\, d\tau \\ &= C_a^m(t) \otimes F \cdot R(t - T_o) \end{aligned} \tag{2.31}$$

Equation 2.31 confirms that if there is a time delay between the measured and the true arterial input curves, the arrival of contrast in the tissue region will be delayed by the same amount of time. As such, the flow-scaled residual function for each of the preceding models can be modified accordingly to account for the delayed arrival of contrast in the tissue region relative to the measured arterial TDC.

For the modified Kety model, $F \cdot R(t)$ in Equation 2.17 is modified to

$$F \cdot R(t - T_o) = F \cdot E \cdot e^{-\frac{FE}{V_e}(t - T_o)} + V_b \cdot \delta(t - T_o) \tag{2.32}$$

For the Patlak model, $F \cdot R(t)$ in Equation 2.18 is modified to

$$F \cdot R(t - T_o) = F \cdot E \cdot H(t - T_o) + V_b \cdot \delta(t - T_o) \tag{2.33}$$

For the J&W model, $F \cdot R(t)$ in Equation 2.24 is changed to

$$F \cdot R(t - T_o) = \begin{cases} 0 & 0 \le t < T \\ F & T_o \le t \le T_o + \mathrm{MTT} \\ F \cdot E \cdot e^{-\frac{FE}{V_e}(t - T_o - \mathrm{MTT})} & t > T_o + \mathrm{MTT} \end{cases} \tag{2.34}$$

2.2.5.4 Dual Hepatic Artery and Portal Vein Input to the Liver

The liver receives approximately two-thirds of its blood supply from the portal vein and the remaining one-third from the common and proper hepatic arteries [40,41]. The portal vein input, $C_p(t)$, can be directly measured if one of the CT slices includes the portal vein in the scan

field of view, while the hepatic artery input, $C_h(t)$, can be approximated by the aortic input at the level of the liver. If we denote α and (1 – α) as the fraction of total blood flow to liver tissue that arises from the hepatic artery (i.e., hepatic arterial fraction) and portal vein, respectively, then $C_a(t)$ can be expressed as the weighted sum of $C_h(t)$ and $C_p(t)$ [42]:

$$C_a(t) = \propto \cdot C_h(t) + (1-\alpha) \cdot C_p(t) \tag{2.35}$$

By replacing $C_a(t)$ in Equation 2.12 with that expressed in Equation 2.35, hepatic arterial fraction can be estimated together with other physiologic parameters using the compartment or J&W model.

2.3 Implementations

After reviewing the theoretical basis of CTP, in this section, an overview of the technical implementations is provided. Discussion will focus on image acquisition and postprocessing, image artifacts commonly seen in CTP studies, typical radiation dose levels of CTP studies, and potential dose reduction techniques for CTP.

2.3.1 Contrast Administration

2.3.1.1 Contrast Medium

Some commonly used nonionic radiographic contrast agents for CTP imaging include Visipaque (Iodixanol, Amersham Health), Omnipaque (Iohexol, GE Healthcare), and Isovue (Iopamidol, Bracco Diagnostic). The typical molecular weight of these agents is about 760 g/mol^{-1} (dalton). The osmolality (solute concentration) of these contrast agents are considered to be low (290–796 mOsm/kg^{-1}) compared to blood plasma. Iodine concentration is available in the range of 140–370 mg iodine/mL, but concentration above 300 should be used for most CTP studies to ensure a good contrast-to-noise ratio of the dynamic images. As the viscosity of contrast media is lower at higher temperature, contrast agent should be warmed to be about the same body temperature (35°C–37°C) before administered to the patient.

2.3.1.2 Contrast Injection Rate

Contrast is usually injected into one of the antecubital veins (e.g., basilica vein) with an injection pump through a 18-gauge cannula taped in place. With a fixed volume of contrast medium, a faster injection rate increases the rate of iodine delivery, which leads to a faster accumulation of contrast material in the aorta and hence a higher arterial enhancement [43]. A faster injection rate also shortens the injection duration and the time to and duration of peak enhancement. The typical bolus injection rate of contrast for CTP is 4–7 mL/s^{-1} [13,14,44–46]. As discussed in Section 2.2.2, a much faster bolus injection is required to satisfy the assumption of no venous outflow if the maximal slope method is used for estimating perfusion. However, an increase in the injection rate greater than 10 mL/s^{-1} is not likely to improve the enhancement further owing to the inherent mixing of contrast medium in the central blood compartment and retrograde reflux, which restricts fast propagation of contrast to the target region [47,48].

If a dual injector is used, a bolus of saline flash of 20–30 mL can be applied following the bolus injection of contrast to push the tail of the iodinated contrast medium into the left ventricle, thus increasing the efficiency of contrast delivery and level of contrast enhancement [47,49]. It can also minimize dispersion and improve the bolus geometry [50]. For CT myocardial perfusion (MP) studies, saline flush may also reduce streak artifacts from the highly attenuating contrast material in the right heart chamber, which may significantly distort the TDC measurement in the interventricular septal wall [51].

2.3.1.3 Contrast Concentration

At a fixed injection rate and volume of contrast medium, a higher concentration delivers a larger dose of iodine, which results in a higher degree of peak contrast enhancement [43]. Therefore, contrast agents with high iodine concentration (320–370 mgI/mL^{-1}) should be used to achieve the highest peak enhancement of the arterial and tissue TDCs to facilitate perfusion map calculation. For MP studies, a more diluted contrast concentration is sometimes preferred to reduce the beam hardening effect arising from the substantial amount of attenuating contrast medium in the left and right heart chambers during the first-pass phase (will be discussed in Section 2.3.5.3). However, iodine concentration below 300 mgI/mL^{-1} is not recommended to avoid suboptimal contrast-to-noise ratio in the images and TDCs.

2.3.1.4 Contrast Volume

Contrast medium is diluted during its passage through circulation. Heavy patients will dilute contrast more due to the fact that those patients have larger blood volume compared to less heavy patients. Thus, the volume of contrast agent used in CTP examinations should be tailored to the patient's body weight. The typical dosage applied at our institution is 0.7 mL/kg^{-1} up to a maximum of 60 mL.